



Simulations of long-range surface plasmon polariton waveguides and devices

Pétur Gordon Hermannsson



**Faculty of Physical Sciences
University of Iceland
2009**

Simulations of long-range surface plasmon polariton waveguides and devices

Pétur Gordon Hermannsson

60 ECTS thesis submitted in partial fulfillment of a
Magister Scientiarum degree in Physics

Advisor
Dr. Kristján Leósson

Faculty Representative
Prof. Snorri Ingvarsson

M.Sc. committee
Dr. Kristján Leósson
Prof. Haflíði P. Gíslason

Faculty of Physical Sciences
School of Engineering and Natural Sciences
University of Iceland
Reykjavík, June 2009

Simulations of long-range surface plasmon polariton waveguides and devices
60 ECTS thesis submitted in partial fulfillment of a *Magister Scientiarum*
degree in Physics

Copyright © 2009 Pétur Gordon Hermannsson
All rights reserved

Faculty of Physical Sciences
School of Engineering and Natural Sciences
University of Iceland
VRII, Hjarðarhagi 2-6
107, Reykjavík
Iceland

Telephone: +354 525 4700

Bibliographic information:

Pétur Gordon Hermannsson, 2009, Simulations of long-range surface plasmon polariton waveguides and devices, Master's thesis, Faculty of Physical Sciences, University of Iceland.

ISBN 978-9979-9953-0-2

Printing: Háskólaprent, Fálkagata 2, 107 Reykjavík
Reykjavík, Iceland, June 2009

Abstract

The properties of long-range surface plasmon polariton waveguides and devices are investigated using the finite element method. In particular, the optical modes of gold stripes and nanowires embedded in a polymer cladding are analyzed as well as how the modes are affected by the waveguide geometry and the resistive heating of the waveguides by a current being passed through the metal cores. This influence of heating on the optical modes can be utilized to realize several active waveguide components, such as variable optical attenuators, adjustable multimode interferometers and directional coupler switches, which are studied in detail. The cross-sectional geometry of the stripe and nanowire waveguides are optimized with respect to coupling to standard single mode optical fibers and waveguide insertion loss. The effect of heating on propagation loss and coupling loss is investigated and transient analysis of the heat transfer is carried out in order to calculate the response times of active device components. The mechanism of attenuation in variable optical attenuators is studied and it is demonstrated how the mode interference in multimode interferometers may be altered by heating in order to realize switching. The influence of cladding geometry on the performance of nanowire waveguides is investigated as well as their tolerance to fabrication errors.

Útdráttur

Eiginleikar ljósrása fyrir langsæknar rafgasbylgjur eru kannaðir með bútaaðferð. Sér í lagi eru sveifluhættir ljósrása sem byggja á málmræmum og nanóvírum úr gulli í fjölleiðklæðningu rannsakaðir ásamt því hvernig lögun málmana og upphitun þeirra með rafstraumi hefur áhrif á sveifluhættina. Þessi tengsl sveifluháttanna við upphitun má nota til að búa til virkar ljósrásir á borð við stillanlega ljósdeyfara, fjölgáttavíxlrásir og stefnutengja, og eru þær rannsakaðar hér. Sú þykkt og breidd málmræmanna og nanovíra sem lágmarkar bæði tapið í ljósrásunum og tapið sem verður þegar ljós er flutt úr hefðbundnum ljósleiðara yfir í ljósrásina er reiknuð. Einnig eru áhrif upphitunar á útbreiðslutap og flutningstap rannsökuð og eru tímaháðir útreikningar gerðir til að finna viðbragðstíma virku ljósrásanna. Deyfingin í stillanlegum ljósdeyfurum er rannsökuð ásamt því hvernig nota megir upphitun til að breyta samliðunarmynstri í fjölgáttavíxlrásum og flytja þannig ljósið frá einni útgangsrás yfir á aðra. Áhrif breiddar og þykktar fjölleiðklæðningarinnar á afkastagetu ljósrása úr nanóvírum er könnuð ásamt þoli þeirra gagnvart framleiðslugöllum.

Contents

List of Figures	xi
List of Tables	xv
Acknowledgements	xvii
1 Introduction	1
2 Theory	5
2.1 Maxwell's equations	5
2.2 The Helmholtz wave equation	7
2.3 The Drude model	7
2.4 The complex refractive index	11
2.5 Surface plasmon polaritons	12
2.5.1 TM modes	14
2.5.2 TE modes	16
2.5.3 Energy confinement and propagation distance	17
2.6 Long range surface plasmon polaritons	18
3 Modeling	27
3.1 The finite element method and COMSOL	27
3.2 PDEs and boundary conditions	30
3.2.1 Heat transfer	30
3.2.2 Eigenmode analysis	31
3.3 Meshing	32
3.4 Application to heated plasmonic waveguides	34

3.4.1	Temperature dependent material properties	34
3.4.2	The modeling of heated waveguides	38
4	Stripe waveguides	43
4.1	Fabrication	43
4.2	Optimization	44
4.3	Heat transfer calculations	48
4.4	Variable optical attenuators	50
4.5	Directional couplers	54
4.6	Multimode interferometers	56
5	Nanowire waveguides	63
5.1	Introduction	63
5.2	Fabrication	65
5.3	Optimization	66
5.4	The influence of cladding on performance	68
5.5	The influence of asymmetry on performance	69
5.6	Heated nanowires	71
6	Conclusion and discussion	75
	Bibliography	79

List of Figures

2.1	The reflectance of copper and gold according to the Drude model.	10
2.2	The real and imaginary part of the complex refractive index of the noble metals.	11
2.3	An electromagnetic wave propagating along the interface between two media.	12
2.4	The dispersion relations of SPPs propagating along the interface between a Drude metal and air and glass.	15
2.5	The calculated evanescent decay length and propagation length for an interface between silver and air.	18
2.6	Surface plasmon polaritons propagating along both sides of a film.	18
2.7	The electric field components of the symmetric mode.	21
2.8	The electric field components of the antisymmetric mode.	22
2.9	The dispersion relation of the symmetric and antisymmetric modes for a 50 nm thick silver film in air.	23
2.10	The behavior of the propagation constant β as a function of film thickness d for a gold film embedded in BCB.	24
3.1	An illustration of the difference between a triangular and a quadrilateral mesh.	33
3.2	The meshed geometry of a stripe waveguide.	34
3.3	The density and thermal conductivity of air as a function of temperature.	35
3.4	The thermal conductivity and heat capacity of gold as a function of temperature.	36
3.5	The thermal conductivity of BCB as a function of temperature.	36

3.6	The refractive index of BCB as a function of wavelength.	37
3.7	The temperature profiles of a gold stripe heated with asymmetric and symmetric cooling conditions.	40
4.1	The fabrication process for LR-SPP waveguides.	44
4.2	An illustration of a LR-SPP stripe waveguide embedded in a polymer.	44
4.3	The simulated and measured cross-sectional intensity profiles of a LR-SPP mode.	45
4.4	The calculated coupling loss, propagation loss and insertion loss for 1 mm long gold stripe waveguides embedded in BCB at $\lambda = 1064$ nm and $\lambda = 1550$ nm.	46
4.5	The calculated intensity profiles along the x -axis compared to measurements on a 10 nm thick, 10.5 μm and 4.5 μm wide waveguide.	47
4.6	The cross-sectional temperature profiles for LR-SPP waveguides in a single and double heatsink configuration, including intensity profiles of the LR-SPP modes.	49
4.7	The asymmetry of the LR-SPP mode for a heat dissipation of 50 mW/mm and asymmetric cooling conditions.	49
4.8	An illustration of a LR-SPP waveguide with contact pads.	50
4.9	The heating of the waveguide leads to a decrease in the real part of the effective mode index of the LR-SPP mode.	51
4.10	The measured extinction ratio of a variable optical attenuator made from a 6 μm wide and 16 nm thick gold stripe with a total length of 2 mm and a 1 mm heated section.	52
4.11	Heating the waveguide leads to increased coupling loss and insertion loss, while decreasing the propagation.	53
4.12	The calculated temporal response of a 15 nm thick and 8 μm wide gold waveguide in BCB heated with an applied power of 50 mW/mm.	54
4.13	A schematic illustration of a directional coupler.	54

4.14	The symmetric and antisymmetric supermodes for two 4 μm wide and 13 nm thick gold stripes embedded in BCB, separated by 2 μm	55
4.15	The calculated coupling length as a function of waveguide separation for two different wavelengths.	56
4.16	An illustration of a tunable multimode interferometer.	57
4.17	The normalized effective mode indices and propagation loss versus waveguide width for a 15 nm thick stripe at $\lambda = 1550$ nm. . .	57
4.18	A schematic illustration of the MMI structure studied.	58
4.19	The modes supported by a $W_{\text{MMI}} = 40$ μm wide MMI device for three different applied heating powers along with the change in effective mode index with increased heating.	59
4.20	Temperature profile of the heated MMI, as determined in COM-SOL.	60
4.21	The calculated intensity of a LR-SPP mode at $\lambda = 1550$ nm propagating through a 40 μm wide and 2.45 mm long MMI with and without 60 mW/mm of applied heating power.	60
5.1	An illustration of the electric field of a fundamental plasmon mode supported by an isolated corner.	63
5.2	The electric field of the four supermodes arising from the coupling of corner modes.	64
5.3	The calculated magnitude and direction of the electric field of the $E^{(0,1)}$ polarized mode in the vicinity of a 180 nm wide gold nanowire in BCB.	65
5.4	The simulated supermodes of a 150 nm wide nanowire made of gold at a wavelength of $\lambda = 1550$ nm.	66
5.5	The calculated coupling loss, propagation loss and fiber-to-fiber insertion loss for 0.5, 1 and 2 mm long gold nanowire waveguides in a 20 μm thick layer of BCB at $\lambda = 1550$ nm.	67
5.6	The coupling loss and propagation loss in symmetric nanowire waveguides for three different cladding thicknesses.	68

5.7	The total insertion loss for different lengths of 180 nm wide symmetric nanowire waveguides when the extent of the dielectric cladding layer is limited vertically and both vertically and horizontally.	69
5.8	The propagation loss and coupling loss in asymmetric nanowire waveguides.	70
5.9	Trapezoidal deformation of the nanowire can result in significant polarization dependent loss.	71
5.10	The real part of the effective mode index for the $E^{(0,1)}$ polarization versus heating power for a gold nanowire in BCB at $\lambda = 1550$ nm.	72
5.11	Heating the waveguide leads to increased coupling loss and insertion loss. The propagation loss decreases however.	73

List of Tables

- 2.1 The free electron densities, relaxation times and corresponding
plasma frequency of the noble metals at room temperature. . . . 10

Acknowledgements

I would like to start by expressing my deepest gratitude towards my advisor Dr. Kristján Leósson for his invaluable guidance throughout the duration of this work. I have found myself in the unique position of having almost unlimited access to my supervisor, something which is exceptionally rare in most academic circles. I would also like to thank Tiberiu Rosenzveig for his collaboration and experimental assistance as well as my other fellow group members.

I am also extremely grateful to my dear wife Gunnur Ýr for her loving support and understanding during the writing this thesis. I also thank my parents and family for their help and kind encouragement throughout my studies.

This project was partially supported by the Icelandic Research Fund and the Icelandic Research Fund for Graduate Students.

1 Introduction

The surge in optical telecommunication in recent years has led to extensive research in the field of integrated optical circuits with the purpose of minimizing device components, reducing cost and realizing various functionalities such as optical routing, splitting etc. Although there is currently no technology that can match optical fibers in transmitting signals over vast distances with low loss, there are however numerous technologies available for guiding over shorter regions, each geared to a particular set of applications. These include waveguides based on semiconductors, polymers, ceramic films and others. However, in recent years more exotic methods of guiding light have been investigated, such as photonic crystal and long-range surface plasmon polaritons waveguides.

It has long been known that an interface between a metal and a dielectric is able to sustain a propagating electromagnetic wave in the form of a surface plasmon polariton (SPP), which arises from interaction between free electrons in the metal and electromagnetic radiation. The most attractive feature of SPPs over conventional dielectric devices is their ability to confine light to below the diffraction limit and realize high field intensities in relatively small volumes. However, due to SPPs being associated with the interface of a metal, a highly lossy material at optical wavelengths, they can only achieve propagation distances of micrometers and have thus not been considered realistic candidates for waveguiding. Instead, they are well suited for sensing applications: the tightly bound nature of SPPs makes them particularly sensitive to changes in refractive index at surfaces [1] and their high field intensities have been employed for example in surface enhanced Raman spectroscopy for single molecule detection [2].

By replacing the single interface with a thin metal film sandwiched between two dielectric layers, the SPPs propagating at each interface can couple to form a symmetric mode, called a long-range surface plasmon polariton (LR-SPP) [3]. As the metal film thickness decreases, the mode evolves into a plane wave in the dielectric, leading to decreased confinement and longer propagation distances. For film thicknesses of the order of 10 nm, propagation distances of tens of millimeters can be achieved at optical wavelengths [4]. Wide metal films are however not suitable for waveguiding since they offer no lateral field confinement and metal stripes (width \gg thickness) are therefore used instead [5]. Furthermore, by adjusting the cross-sectional dimensions of the stripes,

the shape of the fundamental mode can be tuned to closely match that of a standard single mode optical fiber [5, 6, 7], facilitating efficient excitation by end-fire coupling. A number of passive devices and devices components based on LR-SPP waveguides have been experimentally demonstrated, including S-bends, Y-splitters, multimode interferometer devices and directional couplers [8]. However, the main advantage of metal LR-SPP waveguides lies in their ability to conduct an electrical current. By embedding the stripes in claddings with suitable thermo-optic coefficients and resistively heating them, the propagating modes can be altered in order to realize power efficient active devices, such as thermo-optic Mach–Zehnder interferometric modulators and directional coupler switches [9].

Unfortunately, metal films and stripes are only capable of guiding electric fields with the main field component perpendicular to the film. This strong polarization dependence of stripe waveguide components renders them largely incompatible with established integrated optical devices and fibers. In order to address this issue, it has been shown [10, 11, 12] that square metallic nanowires (typically with sidelengths of the order of ~ 200 nm) can support two perpendicularly polarized long-range supermodes and are thus capable of guiding any polarization of light. These supermodes are formed by specific superpositions of plasmon polariton modes that propagate along the corners of the nanowire and can also be efficiently excited by end-fire coupling [12].

Many of the reported SPP devices have been made of gold stripes or nanowires sandwiched between two equally thick layers of the polymer benzocyclobutene (BCB) supported by a silicon substrate. The use of gold is mainly due to its suitable optical properties at telecommunication wavelengths (around $\lambda = 1550$ nm) and the fact that it doesn't form oxides or other compounds at its surface. In order to create power efficient active devices, cladding materials with fairly large (negative) thermo-optic responses are required which makes polymers more suitable than other dielectrics such as glass. Despite other polymers perhaps being more advantageous, BCB has been used in part because of its ease of use and its simple processing, chemical resistance and relatively high glass transition temperature [13] which enables the devices to withstand greater temperatures.

In this thesis the properties of long-range surface plasmon polariton waveguides and devices are investigated using the finite element method. In particular, the optical modes of gold stripes and nanowires embedded in BCB are analyzed as well as how the modes are affected by the waveguide geome-

try and the resistive heating of the waveguides due to a current being passed through the metal cores. Several active devices based on this principle are examined, such as the variable optical attenuator, multimode interferometer and directional coupler. The thesis is organized as follows: first, the behavior of LR-SPPs is theoretically analyzed, followed by a discussion on how the finite element method was used to simulate the waveguides. The results of the simulations are split into two separate chapters, the first dealing with the stripe waveguides and devices and the second with the nanowires. The thesis then ends with a summary and a few concluding remarks regarding the future of LR-SPP research and possible applications.

2 Theory

This chapter lays the theoretical groundwork needed to understand the behavior of long-range surface plasmon polaritons. Starting off with the Maxwell's equations, the necessary equations are derived. The reader is then introduced to the concept of the complex permittivity, and its behavior is investigated with the help of the Drude model of conductivity. Next, following a brief discussion on plasmons, a theoretical analysis is given to the properties of surface plasmon polaritons propagating along an interface between a metal and a dielectric material. Following a similar approach for the case of a double interface, it is shown how the coupling of surface plasmon polaritons on each interface gives rise to long range surface plasmon polaritons.

But as with most discussions on electromagnetic phenomena, we start with the Maxwell's equations.

2.1 Maxwell's equations

The Maxwell's equations are a set of four partial differential equations that can be used to explain all macroscopic electromagnetic phenomena [14]. These can be applied to the interaction of electromagnetic fields with metals of sizes down to a few nanometers without having to resort to the full arsenal of quantum mechanics. This is due to the minute spacing of the energy levels of the conduction electrons compared to the thermal energy at room temperature [15]. The Maxwell's equations are as follows

$$\nabla \cdot \mathbf{D} = \rho_f \quad (2.1)$$

$$\nabla \cdot \mathbf{B} = 0 \quad (2.2)$$

$$\nabla \times \mathbf{E} = -\frac{\partial \mathbf{B}}{\partial t} \quad (2.3)$$

$$\nabla \times \mathbf{H} = \mathbf{J}_f + \frac{\partial \mathbf{D}}{\partial t} \quad (2.4)$$

where \mathbf{D} is the electric displacement, \mathbf{E} is the electric field, \mathbf{B} is the magnetic field and \mathbf{H} is the magnetizing field. These four partial differential equations relate the electric and magnetic fields to their sources: the volume charge density of free charges ρ_f and the density of free current \mathbf{J}_f . Furthermore, the fields are linked via the volume density of electric dipole moment \mathbf{P} and the

volume density of magnetic dipole moment \mathbf{M} by

$$\mathbf{D} = \epsilon_0 \mathbf{E} + \mathbf{P} \quad (2.5)$$

$$\mathbf{H} = \frac{1}{\mu_0} \mathbf{B} - \mathbf{M} \quad (2.6)$$

where ϵ_0 and μ_0 are the electric permittivity and magnetic permeability of vacuum. In the case of linear and isotropic media the polarization and magnetization vectors \mathbf{P} and \mathbf{M} can be written as

$$\mathbf{P} = \epsilon_0 \chi_e \mathbf{E} \quad (2.7)$$

$$\mathbf{M} = \chi_m \mathbf{H} \quad (2.8)$$

where χ_e and χ_m are the electric and magnetic susceptibility of the medium. The electric displacement and magnetic field can then be written as

$$\mathbf{D} = \epsilon_0 (1 + \chi_e) \mathbf{E} \quad (2.9)$$

$$= \epsilon \mathbf{E} \quad (2.10)$$

and

$$\mathbf{B} = \mu_0 (1 + \chi_m) \mathbf{H} \quad (2.11)$$

$$= \mu \mathbf{H} \quad (2.12)$$

where ϵ and μ denote the permittivity and permeability of the medium. Therefore, in the case of linear and isotropic media the Maxwell's equations become

$$\nabla \cdot \mathbf{E} = \frac{\rho_f}{\epsilon} \quad (2.13)$$

$$\nabla \cdot \mathbf{B} = 0 \quad (2.14)$$

$$\nabla \times \mathbf{E} = -\frac{\partial \mathbf{B}}{\partial t} \quad (2.15)$$

$$\nabla \times \mathbf{B} = \mu \mathbf{J}_f + \mu \epsilon \frac{\partial \mathbf{E}}{\partial t} \quad (2.16)$$

Another important constitutive relationship is Ohm's law, which relates the current density \mathbf{J}_f to the electric field \mathbf{E} via the conductivity of the material σ by

$$\mathbf{J}_f = \sigma \mathbf{E} \quad (2.17)$$

2.2 The Helmholtz wave equation

By applying the vector identity $\nabla \times \nabla \times \mathbf{A} = \nabla(\nabla \cdot \mathbf{A}) - \nabla^2 \mathbf{A}$ to equation (2.15), the Maxwell's curl equations can be decoupled, leading to a form of the electromagnetic wave equation.

$$\nabla(\nabla \cdot \mathbf{E}) - \nabla^2 \mathbf{E} = \nabla \times \left(-\frac{\partial \mathbf{B}}{\partial t} \right) \quad (2.18)$$

$$\Rightarrow \quad \nabla^2 \mathbf{E} = \mu\sigma \frac{\partial \mathbf{E}}{\partial t} + \mu\epsilon \frac{\partial^2 \mathbf{E}}{\partial t^2} \quad (2.19)$$

Assuming that the electric field has a harmonic time dependence: $\mathbf{E}(\mathbf{r}, t) = \mathbf{E}(\mathbf{r})e^{-i\omega t}$ then $\frac{\partial}{\partial t} \rightarrow -i\omega$ and equation (2.19) becomes

$$\nabla^2 \mathbf{E}(\mathbf{r}) + \omega^2 \mu \hat{\epsilon} \mathbf{E}(\mathbf{r}) = 0 \quad (2.20)$$

This is known as the Helmholtz equation and $\hat{\epsilon}$ is the so-called complex permittivity

$$\hat{\epsilon} = \epsilon + \frac{i\sigma}{\omega} \quad (2.21)$$

In order to investigate the behavior of the complex permittivity we need a model for σ . A simple description of σ is provided by the Drude model, as explained in the following section.

2.3 The Drude model

The simplest and most commonly used conductivity model is probably the Drude model. It was proposed shortly after the discovery of the electron, and is an application of the kinetic theory of gases to metals. The conduction electrons are considered to behave as a gas of free electrons that move against a background of immobile and heavy positive cores. Under the influence of an external electric field the electrons collide with these cores which leads to a dampening of their motion. The Drude model ignores all interactions that take place between collisions. Furthermore, it assumes that the collisions are instantaneous and that the probability per unit time of an electron experiencing a collision is dt/τ , where τ is the relaxation time [16].

The equation of motion governing the motion of individual electrons is [16]¹

$$m^* \frac{d\mathbf{v}(t)}{dt} = -\frac{m^*}{\tau} \mathbf{v}(t) - e\mathbf{E}(t) \quad (2.22)$$

where m^* is the effective mass of the electrons in the crystal and e is the electronic charge. If the driving field is assumed to have a harmonic time dependence, $\mathbf{E}(t) = \mathbf{E}_0 e^{-i\omega t}$ then equation (2.22) will have a solution of the form $\mathbf{v}(t) = \mathbf{v}_0 e^{-i\omega t}$. Substituting $\mathbf{E}(t)$ into equation (2.22) yields a mean velocity of

$$\mathbf{v}(t) = -\frac{e\tau}{m^*(1 - i\omega\tau)} \mathbf{E}(t) \quad (2.23)$$

The current density is related to the mean velocity of the electrons according to $\mathbf{J}_f = -ne\mathbf{v}$, where n is the number of conduction electrons per unit volume. Therefore

$$\mathbf{J}_f = \frac{ne^2\tau}{m^*(1 - i\omega\tau)} \mathbf{E}(t) \quad (2.24)$$

and comparison with Ohm's law (2.17) gives

$$\sigma = \frac{ne^2\tau}{m^*(1 - i\omega\tau)} \quad (2.25)$$

Using equation (2.21), an expression for the complex permittivity can now be given

$$\hat{\epsilon} = \epsilon - \frac{\omega_p^2 \epsilon_0}{\omega^2 + i\omega/\tau} \quad (2.26)$$

where ω_p is the plasma frequency

$$\omega_p^2 = \frac{ne^2}{\epsilon_0 m^*} \quad (2.27)$$

The first term in equation (2.26) is due to the bound charges in the metal, whereas the second term is due to the free electrons. If the contribution from the bound charges is neglected, the relative complex permittivity ($\hat{\epsilon}_r = \hat{\epsilon}/\epsilon_0$) becomes

$$\hat{\epsilon}_r = 1 - \frac{\omega_p^2}{\omega^2 + i\omega/\tau} \quad (2.28)$$

¹This approach ignores the magnetic field component of the external field \mathbf{B} , as well as the field's \mathbf{r} dependence. As explained by ref. [16], the forces due to \mathbf{B} are many orders of magnitude weaker than those due to the electric field \mathbf{E} . Furthermore, ignoring the \mathbf{r} dependence is safe as long as the field doesn't vary much over distances comparable with the mean free path of the electrons.

Separating this into real and imaginary parts ($\hat{\epsilon}_r = \epsilon'_r + i\epsilon''_r$) gives

$$\epsilon'_r = 1 - \frac{\omega_p^2 \tau^2}{1 + \omega^2 \tau^2} \quad (2.29)$$

$$\epsilon''_r = \frac{\omega_p^2 \tau}{\omega (1 + \omega^2 \tau^2)} \quad (2.30)$$

The relaxation time τ is typically of the order 10^{-15} to 10^{-14} seconds at room temperature [16]. For visible and shorter wavelengths $\omega\tau \gg 1$ and the real part may be approximated as

$$\epsilon'_r \approx 1 - \frac{\omega_p^2}{\omega^2} \quad (2.31)$$

At frequencies lower than the plasma frequency, $\omega < \omega_p$, ϵ'_r becomes negative and the solution to the Helmholtz equation (2.20) decays exponentially in space, leading to the metal being highly reflective. However, when $\omega > \omega_p$, ϵ'_r becomes positive and the solution to (2.20) become oscillatory and the metal is transparent. From this we can see that the plasma frequency may therefore be interpreted as the frequency at which the metal starts becoming transparent to incoming electromagnetic radiation. Furthermore, it can be shown [15, 16] that the plasma frequency corresponds to the characteristic frequency of collective longitudinal oscillations of the free electron gas. The quanta of these plasma oscillations are known as (volume or bulk) *plasmons*, and due to their longitudinal nature, they do not couple to transverse electromagnetic waves. Surface plasmons on the other hand couple readily to photons to form polaritons, as we shall see later.

The plasma frequency of most metals is in the ultraviolet part of the spectrum, which explains why they are reflective at visible wavelengths. Table 2.1 shows the plasma frequency and the corresponding wavelength for the three noble metals (copper, silver and gold), as obtained from equation (2.27) using $m^* = m_e$ and data on the free electron densities n and relaxation times τ from ref. [16]. The reflectivity spectrum of gold and copper according to the Drude model is shown in figure 2.1, in which the dashed lines indicate the plasma frequency for each metal.

Table 2.1: The free electron densities and relaxation times of the noble metals at room temperature [16], and the corresponding calculated plasma frequency and wavelength.

Element	n [10^{22} cm $^{-3}$]	τ [fs]	ω_p [10^{16} s $^{-1}$]	λ nm
Copper	8.47	27	1.643	115
Silver	5.86	40	1.365	138
Gold	5.90	30	1.370	138

It is worth pointing out however that the Drude model doesn't accurately describe the behavior of many metals at high frequencies, as is evident by the apparent difference in color between gold and silver despite having the same plasma frequency. The alkali metals such as lithium, sodium and potassium do indeed have an almost Drude-like response and become transparent in the ultraviolet, but in the case of the noble metals, absorption due to interband transitions becomes increasingly important for visible frequencies. Nevertheless, the Drude model remains popular due to its simplicity and can be easily modified to correctly describe the optical properties of gold and silver [15]. For our purposes however, the Drude model in its present form is adequate.

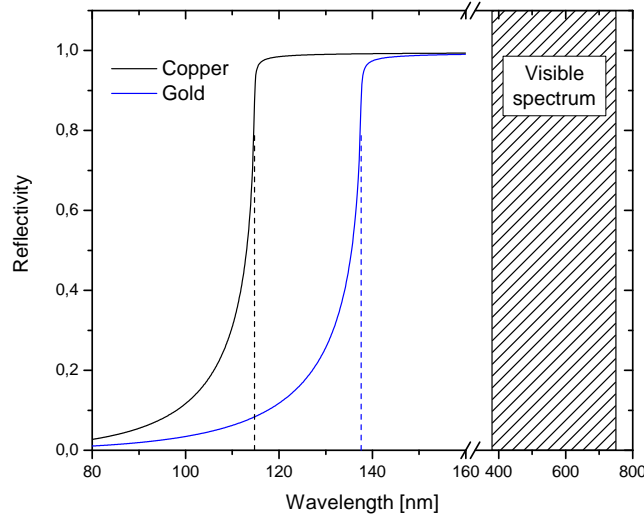


Figure 2.1: The reflectance of copper and gold according to the Drude model.

2.4 The complex refractive index

It can sometimes be more convenient to use the complex refractive index $\tilde{n} = n + i\kappa$ instead of the complex permittivity $\hat{\epsilon}_r = \epsilon'_r + i\epsilon''_r$. The complex refractive index is defined as $\tilde{n} = \sqrt{\hat{\epsilon}_r}$, which gives

$$n^2 = \frac{\sqrt{\epsilon'^2_r + \epsilon''^2_r} + \epsilon'_r}{2} \quad (2.32)$$

$$\kappa^2 = \frac{\sqrt{\epsilon'^2_r + \epsilon''^2_r} - \epsilon'_r}{2} \quad (2.33)$$

Here, n corresponds to the traditional index of refraction, while κ is the so-called extinction coefficient and determines the absorption loss of an electromagnetic wave as it propagates through a material. It is related to the absorption coefficient α of Beer's law $I(z) = I_0 e^{-\alpha z}$ via

$$\alpha = \frac{2\kappa\omega}{c} \quad (2.34)$$

where I is the intensity of a propagating wave, which is attenuated exponentially due to the medium. Figure 2.2 shows the real and imaginary components of \tilde{n} for the three noble metals.

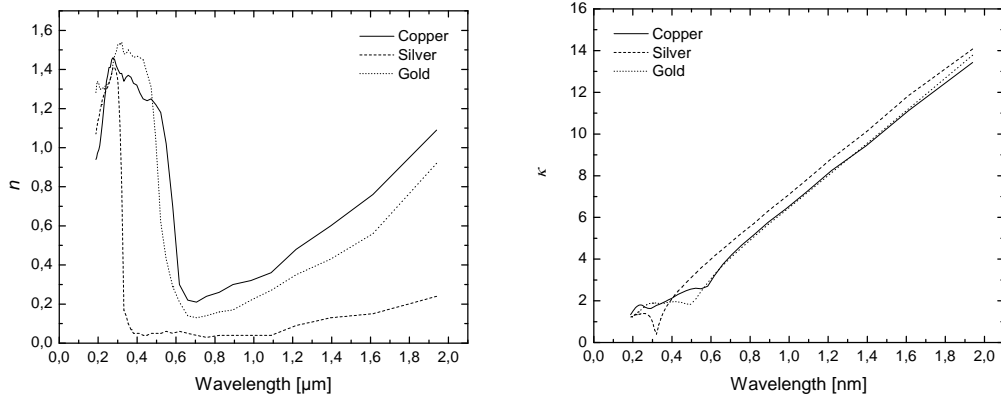


Figure 2.2: The real (left) and imaginary part (right) of the complex refractive index of the noble metals. The figure is adapted from data published in ref. [17].

2.5 Surface plasmon polaritons

We will now investigate the possibility of an electromagnetic wave propagating along the interface between two materials. For the sake of simplicity, we will consider the case where the permittivity $\hat{\epsilon}$ only varies in one spatial coordinate, $\hat{\epsilon} = \hat{\epsilon}(z)$. The interface is set to coincide with $z = 0$ and the wave propagation is taken to be in the x direction, showing no spatial variation in the in-plane y -direction. The geometry along with the propagating wave is illustrated in figure 2.3.

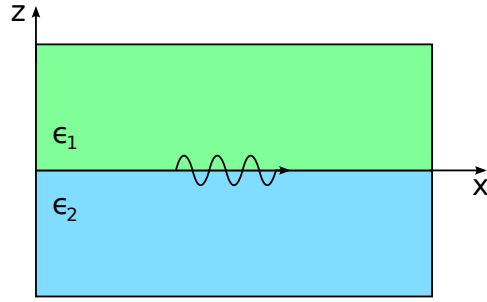


Figure 2.3: An electromagnetic wave propagating along the interface between two media.

The propagating wave can be written as $\mathbf{E}(\mathbf{r}, t) = \mathbf{E}(z)e^{i(\beta x - \omega t)}$, where β is the propagation constant of the traveling wave. It is a complex parameter and corresponds to the component of the wave vector in the direction of propagation [15]. It is related to the effective mode index n_{eff} of a waveguide via

$$\beta = n_{\text{eff}} \frac{2\pi}{\lambda} \quad (2.35)$$

where λ is the wavelength. Inserting the expression for the propagating wave into Helmholtz equation (2.20) yields

$$\frac{\partial^2 \mathbf{E}(z)}{\partial z^2} + (\omega^2 \mu \hat{\epsilon} - \beta^2) \mathbf{E}(z) = 0 \quad (2.36)$$

Now, since the wave is assumed to have a harmonic time dependence $e^{-i\omega t}$, the two Maxwell's equations (2.15) and (2.16) become

$$\nabla \times \mathbf{E} = i\omega \mathbf{B} \quad (2.37)$$

$$\nabla \times \mathbf{B} = -i\omega \mu \hat{\epsilon} \mathbf{E} \quad (2.38)$$

Due to both the propagation being in the x -direction $\frac{\partial}{\partial x} \rightarrow i\beta$ and the lack of

spatial variation in the y -direction $\frac{\partial}{\partial y} \rightarrow 0$, these two curl equations lead to the following coupled equations:

$$\frac{\partial B_y}{\partial z} = i\omega\mu\hat{\epsilon}E_x \quad (2.39)$$

$$i\beta B_y = -i\omega\mu\hat{\epsilon}E_z \quad (2.40)$$

$$\frac{\partial E_x}{\partial z} - i\beta E_z = i\omega B_y \quad (2.41)$$

$$\frac{\partial E_y}{\partial z} = -i\omega B_x \quad (2.42)$$

$$i\beta E_y = i\omega B_z \quad (2.43)$$

$$\frac{\partial B_x}{\partial z} - i\beta B_z = -i\omega\mu\hat{\epsilon}E_y \quad (2.44)$$

According to ref. [15], these equations allow for two sets of self-consistent solutions with different polarization properties of the propagating waves. The first three correspond to transverse magnetic (TM) modes, where only the field components E_x , E_z and B_y are nonzero, and the last three correspond to transverse electric (TE) modes where only B_x , B_z and E_y are nonzero.

In the case of TM modes, the above equations reduce to

$$E_x = -i\frac{1}{\omega\mu\hat{\epsilon}}\frac{\partial B_y}{\partial z} \quad (2.45)$$

$$E_z = -\frac{\beta}{\omega\mu\hat{\epsilon}}B_y \quad (2.46)$$

$$\frac{\partial^2 B_y}{\partial z^2} + (\omega^2\mu\hat{\epsilon} - \beta^2) B_y = 0 \quad (2.47)$$

whereas in the case of TE modes they reduce to

$$B_x = \frac{i}{\omega}\frac{\partial E_y}{\partial z} \quad (2.48)$$

$$B_z = \frac{\beta}{\omega}E_y \quad (2.49)$$

$$\frac{\partial^2 E_y}{\partial z^2} + (\omega^2\mu\hat{\epsilon} - \beta^2) E_y = 0 \quad (2.50)$$

Now, having determined the governing equations for both the TE and TM modes, we are ready to turn our attention back to the problem at hand. We

will first examine the properties of a TM polarized wave propagating along the interface.

2.5.1 TM modes

In the region $z > 0$, where the permittivity and permeability are $\hat{\epsilon}_1$ and μ_1 respectively, equation (2.47) has the solution $B_y = Ae^{-k_1 z}$, where A is a coefficient describing the amplitude and k_1 is the component of the wave vector perpendicular to the interface in this medium, $k_1^2 = \beta^2 - \omega^2 \mu_1 \hat{\epsilon}_1$. Tagging on the propagation factor $e^{i\beta x}$ then gives

$$B_y = Ae^{-k_1 z} e^{i\beta x} \quad (2.51)$$

Furthermore, from equations (2.45) and (2.46) we obtain

$$E_x = iA \frac{k_1}{\omega \mu_1 \hat{\epsilon}_1} e^{-k_1 z} e^{i\beta x} \quad (2.52)$$

$$E_y = -A \frac{\beta}{\omega \mu_1 \hat{\epsilon}_1} e^{-k_1 z} e^{i\beta x} \quad (2.53)$$

Similarly, in the region $z < 0$, we get

$$B_y = Be^{k_2 z} e^{i\beta x} \quad (2.54)$$

$$E_x = -iB \frac{k_2}{\omega \mu_2 \hat{\epsilon}_2} e^{k_2 z} e^{i\beta x} \quad (2.55)$$

$$E_y = -B \frac{\beta}{\omega \mu_2 \hat{\epsilon}_2} e^{k_2 z} e^{i\beta x} \quad (2.56)$$

where $k_2^2 = \beta^2 - \omega^2 \mu_2 \hat{\epsilon}_2$ and B is a second amplitude coefficient.

In the absence of a surface current and assuming that both materials are non-magnetic, $\mu_1 = \mu_2 = \mu_0$, the tangential field components B_y and E_x must be continuous across the interface. This requires that $A = B$, and more importantly that

$$\frac{k_1}{k_2} = -\frac{\hat{\epsilon}_1}{\hat{\epsilon}_2} \quad (2.57)$$

In order for the surface wave to be confined to the interface, the real parts of k_1 and k_2 must be positive, which in turn requires that the real parts of the complex permittivities $\hat{\epsilon}_1$ and $\hat{\epsilon}_2$ are opposite in sign. As discussed in section 2.3, for most metals the real part of $\hat{\epsilon}$ becomes negative for visible and longer wavelengths, and thus an interface between a dielectric and a metal satisfies

this condition. A confined surface wave propagating along such an interface is called a *surface plasmon polariton* (SPP) and arises via the coupling of the electromagnetic field to surface plasmons [15] (see below). By combining the expressions for k_1 and k_2 with equation (2.57) we obtain the dispersion relation of the SPPs

$$\beta = \frac{\omega}{c} \sqrt{\frac{\hat{\epsilon}_{r1} \hat{\epsilon}_{r2}}{\hat{\epsilon}_{r1} + \hat{\epsilon}_{r2}}} \quad (2.58)$$

By assuming that $\hat{\epsilon}_{r1}$ is real ($\hat{\epsilon}_{r1} = \epsilon_{r1}$) and that the condition $\epsilon''_{r2} < |\epsilon'_{r2}|$ holds for $\hat{\epsilon}_{r2} = \epsilon'_{r2} + i\epsilon''_{r2}$, the real and imaginary parts of the propagation constant $\beta = \beta' + i\beta''$ can be separated [18]

$$\beta' = \frac{\omega}{c} \left(\frac{\epsilon_{r1} \epsilon'_{r2}}{\epsilon_{r1} + \epsilon'_{r2}} \right)^{1/2} \quad (2.59)$$

$$\beta'' = \frac{\omega}{c} \left(\frac{\epsilon_{r1} \epsilon'_{r2}}{\epsilon_{r1} + \epsilon'_{r2}} \right)^{3/2} \frac{\epsilon''_{r2}}{2(\epsilon'_{r2})^2} \quad (2.60)$$

Figure 2.4 shows plots of equation (2.58) for interfaces between air (blue, $\hat{\epsilon}_{r1} = 1$) and glass (red, $\hat{\epsilon}_{r1} = 1.5^2$) and a Drude metal with negligible absorption (i.e. $\epsilon''_{r2} = 0$) and a relative permittivity as given in equation (2.31). The solid lines indicate the real parts of the propagation constant, whereas the

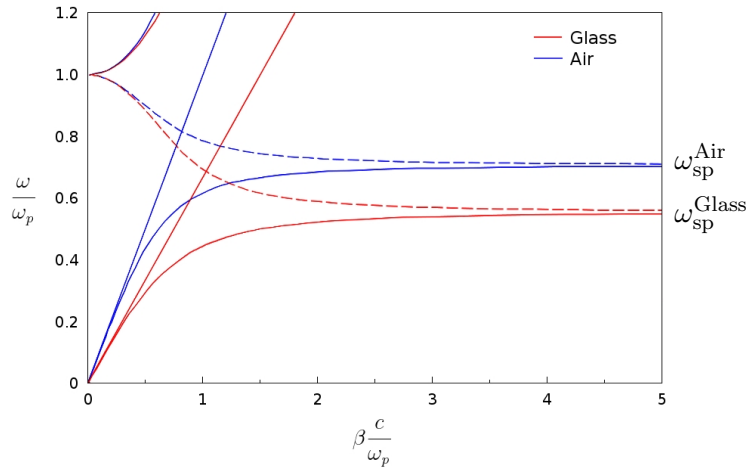


Figure 2.4: The dispersion relations of SPPs propagating along the interface between a Drude metal and air and glass.

dashed lines indicate the imaginary parts. The straight lines in the figure are the lightlines, which are the dispersion curves the light would follow were it free to propagate through the dielectric medium, $\beta_0 = (\omega/c)\sqrt{\hat{\epsilon}_{r1}}$. The solid curves in the upper left corner are the quasibound, leaky modes [15].

As can be seen from figure 2.4, as the frequency decreases the propagation constant tends to β_0 and the SPP mode becomes increasingly less confined to the interface until it eventually acquires the nature of a grazing-incidence light field, known as Sommerfeld-Zenneck waves [15]. On the other hand, as the propagation constant increases, the frequency of the SPPs approaches the characteristic surface plasmon frequency

$$\omega_{\text{sp}} = \frac{\omega_p}{\sqrt{1 + \hat{\epsilon}_1}} \quad (2.61)$$

In this regime, the group velocity $v_g = d\omega/d\beta \rightarrow 0$ and the mode acquires an electrostatic character, and is known as a surface plasmon [15].

By inspection of equation (2.58), it can be seen that $\beta > \beta_0$, and the dispersion curves of SPPs always lie to the right of their respective light lines. The SPPs therefore cannot transform into light and are said to be non-radiative. Conversely, the opposite is also true; SPPs cannot be excited by simply irradiating the interface with light. Some method of increasing the propagation constant of the light must be used, such as grating or prism coupling [15, 19] or scattering from surface roughness or defects [15, 18, 20]. A point source of SPPs has also been shown to be generated on gold and silver films by the optical probe of a scanning near-field optical microscope [21].

2.5.2 TE modes

Let us now briefly investigate the case of TE surface modes. In a completely analogous manner as before, equation (2.50) yields a confined wave solution of the form $E_y = A \exp(-k_1 z) \exp(i\beta x)$ in the region $z > 0$ and $E_y = B \exp(k_2 z) \exp(i\beta x)$ in the region $z < 0$. Continuity at the boundary $z = 0$ demands that $A = B$. Inserting these expressions into equation (2.48) gives

$$B_x = \begin{cases} -A \frac{ik_1}{\omega} e^{-k_1 z} e^{i\beta x} & z > 0 \\ A \frac{ik_2}{\omega} e^{k_2 z} e^{i\beta x} & z < 0 \end{cases} \quad (2.62)$$

From the condition that B_x must also be continuous across the interface we get

$$k_1 + k_2 = 0 \quad (2.63)$$

but in order for the wave to be confined to the interface, it is necessary that $\text{Re}(k_1), \text{Re}(k_2) > 0$, which is inconsistent with this condition. Surface plasmon polaritons therefore cannot exist in a TE polarized state.

2.5.3 Energy confinement and propagation distance

Two important quantities that characterize SPPs are the evanescent decay length \hat{z} and propagation length L . The evanescent decay length quantifies the confinement of the surface wave and is defined as the distance from the interface where the magnitude of the fields has dropped to $1/e$

$$\hat{z} = \frac{1}{|k_i|} \quad i = 1, 2 \quad (2.64)$$

Therefore, the larger the decay length, the weaker the confinement. Similarly, L is where the intensity of the propagating wave has dropped to $1/e$

$$L = \frac{1}{2\text{Im}(\beta)} \quad (2.65)$$

In the visible regime, L is typically in the range of a few μm , depending on which metal and dielectric form the interface [15].

Both \hat{z} and L depend strongly on the frequency, as is evident from the dispersion relation. As shown in figure 2.4, both the real and imaginary parts of β blow up as the frequency approaches the surface plasmon frequency ω_{sp} , leading to large values of k_i and thus high confinement on the one hand, and short propagation distances on the other. This trade-off between confinement and loss is typical for plasmonics. According to equation (2.60), the highest propagation lengths are realized for low frequencies and low $\epsilon''_{r2}/(\epsilon'_{r2})^2$ ratios, and as we shall see in the next section, introducing a second interface can increase the propagation lengths even further.

Figure 2.5 shows the predicted behavior of the evanescent decay length and propagation length for an interface between silver and air, using previously published data on the optical properties of silver [17]. The results are compared to the evanescent decay length and propagation length obtained by modeling the silver as a Drude metal ($\omega_p = 1.365 \cdot 10^{16} \text{ s}^{-1}$ and $\tau = 40 \text{ fs}$). The figure clearly shows how increased confinement diminishes the propagation length.

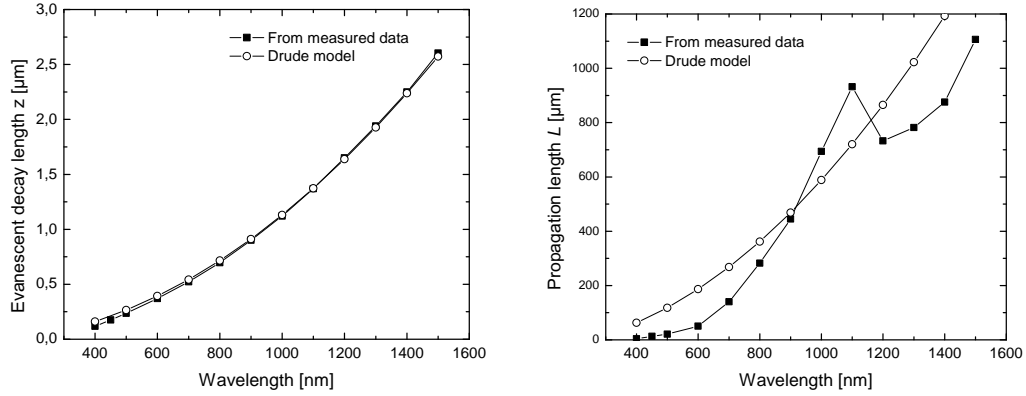


Figure 2.5: The calculated evanescent decay length and propagation length for an interface between silver and air. Increasing the wavelength decreases the confinement of the SPP mode while simultaneously allowing it to propagate further. The evanescent decay length calculated for the measured data is in particularly good agreement with the results obtained from the Drude model.

2.6 Long range surface plasmon polaritons

We now turn our attention to what happens when a second interface capable of sustaining SPPs is added to the system. In particular, we will study the case of a thin metallic film sandwiched between two dielectrics, as shown in figure 2.6. It turns out that when the separation between the interfaces becomes comparable to or smaller than the evanescent decay length \hat{z} , the SPPs on each interface start to interact, giving rise to coupled modes with several interesting properties. To simplify matters, the discussion will be limited to the symmetric case, where the refractive index of the dielectric on both sides

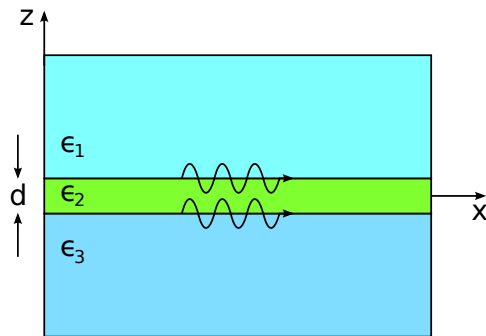


Figure 2.6: Surface plasmon polaritons propagating along both sides of a film.

of the film is the same, $\hat{\epsilon}_{r_1} = \hat{\epsilon}_{r_3}$.

In the previous analysis of a single interface it was shown that surface plasmons can only exist in the TM polarized state. The governing equations were found to be (repeated for convenience)

$$E_x = -i \frac{1}{\omega \mu \hat{\epsilon}} \frac{\partial B_y}{\partial z} \quad (2.45)$$

$$E_z = -\frac{\beta}{\omega \mu \hat{\epsilon}} B_y \quad (2.46)$$

$$\frac{\partial^2 B_y}{\partial z^2} + (\omega^2 \mu \hat{\epsilon} - \beta^2) B_y = 0 \quad (2.47)$$

As before, in the regions above and below the film, the TM wave equation (2.47) has solutions that decay exponentially away from the interfaces

$$B_y = \begin{cases} A e^{-k_1(z-d/2)} e^{i\beta x} & z > d/2 \\ B e^{k_1(z+d/2)} e^{i\beta x} & z < -d/2 \end{cases}$$

$$\text{where } k_1^2 = \beta^2 - \omega^2 \mu_1 \hat{\epsilon}_1 \quad (2.66)$$

However, in the film region $-d/2 < z < d/2$ the modes localized at each interface couple, yielding

$$B_y = C e^{k_2(z-d/2)} e^{i\beta x} + D e^{-k_2(z+d/2)} e^{i\beta x}$$

$$\text{where } k_2^2 = \beta^2 - \omega^2 \mu_2 \hat{\epsilon}_2 \quad (2.67)$$

Now, with the help of equations (2.45) and (2.46), the remaining field components E_x and E_z can be calculated to give the following set of equations. Since all the field components have the spatial dependence on x , the propagation factor $e^{i\beta x}$ has been omitted for the sake of clarity.

$$\left. \begin{aligned} B_y &= Ae^{-k_1(z-d/2)} \\ E_x &= iA \frac{k_1}{\omega\mu_1\hat{\epsilon}_1} e^{-k_1(z-d/2)} \\ E_z &= -A \frac{\beta}{\omega\mu_1\hat{\epsilon}_1} e^{-k_1(z-d/2)} \end{aligned} \right\} \quad z > d/2$$

$$\left. \begin{aligned} B_y &= Ce^{k_2(z-d/2)} + De^{-k_2(z+d/2)} \\ E_x &= -\frac{i}{\omega\mu_2\hat{\epsilon}_2} (Ck_2e^{k_2(z-d/2)} - Dk_2e^{-k_2(z+d/2)}) \\ E_z &= -\frac{\beta}{\omega\mu_2\hat{\epsilon}_2} (Ce^{k_2(z-d/2)} + De^{-k_2(z+d/2)}) \end{aligned} \right\} \quad -d/2 < z < d/2$$

$$\left. \begin{aligned} B_y &= Be^{k_1(z+d/2)} \\ E_x &= -iB \frac{k_1}{\omega\mu_1\hat{\epsilon}_1} e^{k_1(z+d/2)} \\ E_z &= -B \frac{\beta}{\omega\mu_1\hat{\epsilon}_1} e^{k_1(z+d/2)} \end{aligned} \right\} \quad z < -d/2$$

For non-magnetic media ($\mu_1 = \mu_2 = \mu_0$), the tangential components of the \mathbf{E} and \mathbf{B} fields must be continuous at the interfaces. Applying these boundary conditions at $z = \pm d/2$ leads to the following set of linear equations

$$\begin{aligned} z = +d/2 : \quad A &= C + De^{-k_2d} \\ \frac{k_1}{\hat{\epsilon}_1} A &= -\frac{k_2}{\hat{\epsilon}_2} C + \frac{k_2}{\hat{\epsilon}_2} De^{-k_2d} \\ z = -d/2 : \quad B &= Ce^{-k_2d} + D \\ \frac{k_1}{\hat{\epsilon}_1} B &= \frac{k_1}{\hat{\epsilon}_1} Ce^{-k_2d} - \frac{k_2}{\hat{\epsilon}_2} D \end{aligned}$$

which can be more clearly expressed in matrix form

$$\begin{vmatrix} 1 & 0 & -1 & e^{-k_2d} \\ 0 & 1 & -e^{-k_2d} & -1 \\ \frac{k_1}{\hat{\epsilon}_1} & 0 & \frac{k_2}{\hat{\epsilon}_2} & -\frac{k_2}{\hat{\epsilon}_2} e^{-k_2d} \\ 0 & \frac{k_1}{\hat{\epsilon}_1} & -\frac{k_2}{\hat{\epsilon}_2} e^{-k_2d} & \frac{k_2}{\hat{\epsilon}_2} \end{vmatrix} \begin{vmatrix} A \\ B \\ C \\ D \end{vmatrix} = \mathbf{0} \quad (2.68)$$

This is a matrix equation of the form $M\mathbf{b} = \mathbf{0}$. In order for it to have a non-trivial solution, the determinant $\det(M)$ must be zero (otherwise M would be invertible and $\mathbf{b} = M^{-1}\mathbf{0} = \mathbf{0}$). Setting the determinant to zero gives the following condition

$$e^{-k_2 d} = \pm \frac{k_1/\hat{\epsilon}_1 + k_2/\hat{\epsilon}_2}{k_1/\hat{\epsilon}_1 - k_2/\hat{\epsilon}_2} \quad (2.69)$$

which implicitly links the propagation constant β and frequency ω via k_1 and k_2 . In other words, it is the dispersion relation for the coupled SPP mode. Note that if $d \rightarrow \infty$ we recover the condition for the existence of a surface plasmon polariton on a single interface (2.57).

If the negative solution of equation (2.69) is inserted into the matrix equation (2.68), it can be solved for the constants A through D . After some algebra we arrive at the following solution for the magnetic field component B_y . Here the constant A has been normalized to $A = 1$.

$$B_y = \begin{cases} e^{-k_1(z-d/2)} e^{i\beta x} & z > d/2 \\ -\frac{\sqrt{(k_2/\hat{\epsilon}_2)^2 - (k_1/\hat{\epsilon}_1)^2}}{k_2/\hat{\epsilon}_2} e^{i\beta x} \cosh(k_2 z) & -d/2 < z < d/2 \\ e^{k_1(z+d/2)} e^{i\beta x} & z < -d/2 \end{cases} \quad (2.70)$$

This mode is therefore symmetric with respect to the center of the film and corresponds to a *long-range surface plasmon polariton* (LR-SPP) as we shall see later. Because of their relatively large propagation lengths, LR-SPPs are of significant practical importance such as in waveguiding, which is indeed the main focus of this thesis. According to equations (2.45) and (2.46), the electric field components E_x and E_z are antisymmetric and symmetric, respectively, as shown in figure 2.7. It should be noted that the figure is only intended to

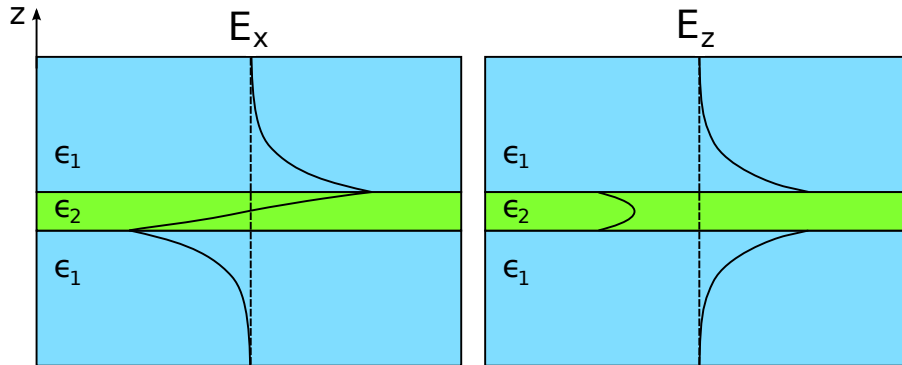


Figure 2.7: The electric field components of the symmetric mode.

give the reader a feel for the shape of the fields and are therefore not to scale. However, from equations (2.45) and (2.46) it can be seen that in the dielectric $|E_z/E_x| = \beta/k_1$, and since β is always greater than k_1 (see equation (2.66)), E_z is the dominant component.

Let us now investigate the mode that arises from the positive solution of equation (2.69). Solving equation (2.68) and setting $A = 1$ as before, produces

$$B_y = \begin{cases} e^{-k_1(z-d/2)} e^{i\beta x} & z > d/2 \\ -\frac{\sqrt{(k_1/\epsilon_1)^2 - (k_2/\epsilon_2)^2}}{k_2/\epsilon_2} e^{i\beta x} \sinh(k_2 z) & -d/2 < z < d/2 \\ -e^{k_1(z+d/2)} e^{i\beta x} & z < -d/2 \end{cases} \quad (2.71)$$

which is antisymmetric with respect to the center of the film and corresponds to a *short-range surface plasmon polariton* (SR-SPP). In this case, E_x and E_z are symmetric and antisymmetric, as shown in figure 2.8.

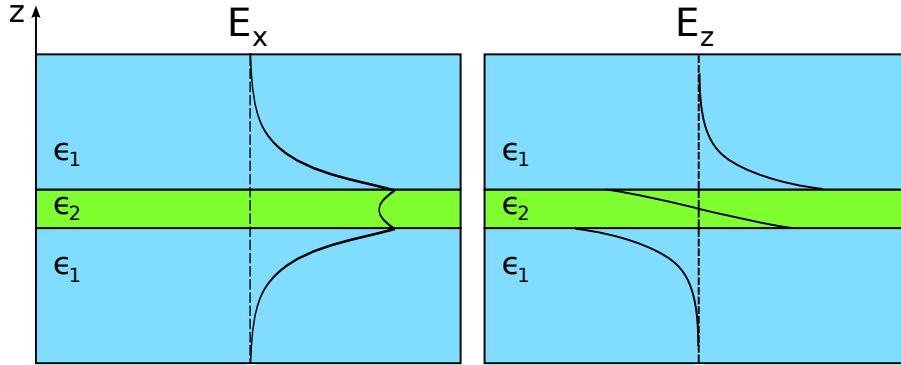


Figure 2.8: The electric field components of the antisymmetric mode.

Figure 2.9 shows the dispersion relations of both the symmetric and symmetric modes for a $d = 50$ nm thick silver film in air. The silver is modelled as a Drude metal with a plasma frequency of $\omega_p = 1.4 \cdot 10^{16}$ rad/s and a purely real relative permittivity described by equation (2.31). The figure also shows the dispersion curve of a SPP propagating along a single interface. As we can see, the symmetric mode diverges more slowly from the light line than both the single interface mode and the antisymmetric mode, making it less confined to the film and thus propagating further than the two other modes.

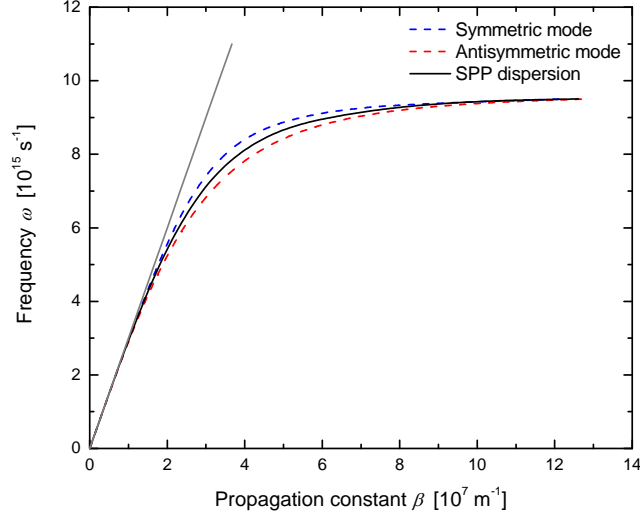


Figure 2.9: The dispersion relation of the symmetric and antisymmetric modes for a 50 nm thick silver film in air. The dispersion relation of a single interface is also shown.

It is also particularly instructive to investigate the dependence of the propagation constant β on the metal film thickness d . The dispersion relation (2.69) was numerically solved for β as a function of d for the case of a gold film embedded in the polymer benzocyclobutene (BCB) at a wavelength of $\lambda = 1550$ nm. These materials are chosen since LR-SPP waveguides quite commonly consist of gold stripes in BCB claddings, as mentioned in the introduction. The value of the relative complex permittivity of gold at this wavelength was interpolated from data published in ref. [17] and found to be $\hat{\epsilon}_{r_2} = -114.9 - 11.2i$, while the dielectric constant of BCB is given by its manufacturer to be $\epsilon_{r_1} = 1.535^2$. The results are shown in figure 2.10, where the real and imaginary parts of β have been normalized with respect to the free space propagation constant $k_0 = 2\pi/\lambda$ and plotted separately. The figures illustrate how the SPP mode of a single interface branches into a symmetric (β_s) and antisymmetric (β_a) mode as the metal film thickness is reduced. In the case of the antisymmetric mode, both the real and imaginary parts of β_a increase rapidly with decreasing film thickness, leading to strong field confinement and thus short propagation lengths according to equations (2.64) and (2.65).

As can be seen from figure 2.10b, the propagation length of the antisymmetric mode can become several orders of magnitude shorter than the propagation length of single interface SPPs, and is thus often termed a short-range surface

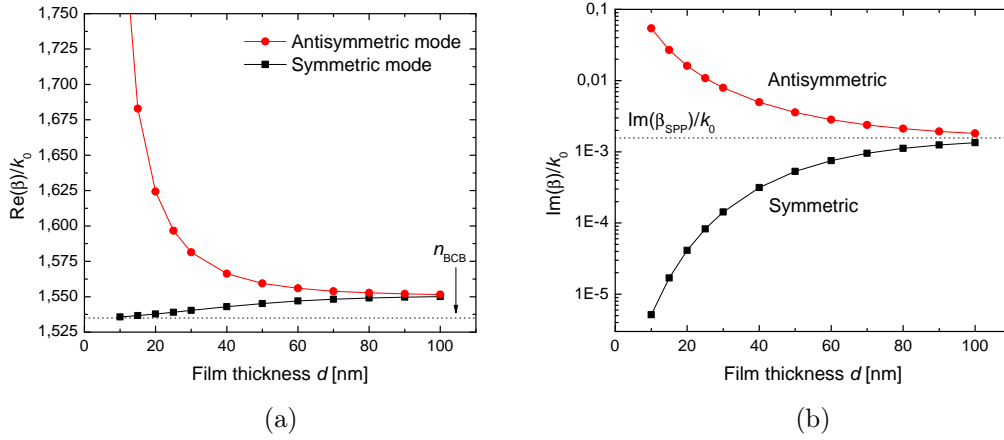


Figure 2.10: The behavior of the propagation constant β as a function of film thickness d for a gold film embedded in BCB. As the film thickness decreases the propagation constant of a single interface branches into a symmetric and antisymmetric mode.

plasmon polariton. Conversely, as the film thickness is reduced, the real part of β_s for the symmetric mode tends towards the propagation constant of a freely propagating plane wave in the dielectric whereas the imaginary part decreases rapidly, leading to vastly improved propagation lengths compared to the single interface mode. For this reason the symmetric mode has acquired the name of long-range surface plasmon polariton.

This behavior can be further understood by inspection of the dispersion relation in equation (2.69). Setting $d \rightarrow 0$ in the symmetric case (negative solution) yields that $k_1 \rightarrow 0$ and thus $\beta \rightarrow (\omega/c)\sqrt{\epsilon_{r1}}$ in equation (2.66). The propagation constant therefore approaches that of a freely propagating plane wave in the dielectric, as mentioned before. Recalling that the propagation length L of the mode (2.65) is inversely proportional to the imaginary part of β , we see that as $\beta \rightarrow (\omega/c)\sqrt{\epsilon_{r1}}$, the imaginary part of β goes to zero in the case of lossless dielectrics, and $L \rightarrow \infty$. In the case of lossy dielectrics, the attenuation is asymptotic to plane wave loss in these media. These are the long-range surface plasmon polaritons mentioned above and their existence was first demonstrated by Sarid in 1981 [3]. However, since the field intensities are greatest at the interfaces, the LR-SPPs are very sensitive to surface properties [18]. Therefore, when the metal thickness is down to a few nanometers, effects such as surface roughness and grain size in the metal start playing an increased role and the mode never becomes completely lossless. In the case of the antisymmetric mode, corresponding to short-range surface plasmon polaritons

(positive solution), when $d \rightarrow 0$, then $k_2 \rightarrow 0$ and therefore $\beta \rightarrow (\omega/c)\sqrt{\hat{\epsilon}_{r_2}}$, which is the propagation constant of a wave propagating through the metal. As discussed in section 2.3, most metals are opaque at visible and higher wavelengths and the SR-SPPs are therefore very quickly attenuated.

An equivalent way of looking at this is to consider the confinement. In the antisymmetric case, as $d \rightarrow 0$ then $\beta \rightarrow (\omega/c)\sqrt{\hat{\epsilon}_{r_2}}$ as before, which leads to $k_1 \rightarrow (\omega/c)\sqrt{\hat{\epsilon}_{r_2} - \epsilon_{r_1}} \neq 0$ in equation (2.66). In the symmetric case $\beta \rightarrow (\omega/c)\sqrt{\epsilon_{r_1}}$ as $d \rightarrow 0$, which means that $k_1 \rightarrow 0$. Since k_1 quantifies the confinement of the mode, the field is obviously more confined in the antisymmetric mode and thus more energy is carried and dissipated by the lossy metal than in the symmetric case, where the dissipation from the metal is reduced.

In addition to LR-SPPs having a significantly longer propagation length than their single interface counterparts, they don't have to be excited via inconvenient means such as gratings or prisms. Instead, due to their symmetry, LR-SPPs can be excited efficiently by end-fire coupling (a well known technique in integrated optics) by matching an incident light field to the LR-SPP mode [4].

So far, we have only considered the case where the permittivity $\hat{\epsilon}$ varies in one spatial coordinate, $\hat{\epsilon} = \hat{\epsilon}(z)$, in particular an infinitely wide metal film sandwiched between identical dielectric layers. Such configurations are of limited practical interest since a propagating wave will spread out laterally away from its source due to the confinement only being along the vertical axis. In the year 2000, Berini was the first to theoretically demonstrate that metal films of finite width were capable of guiding LR-SPPs, offering two-dimensional confinement to the modes [5]. Although these metal stripes have a relatively simple geometry, their modes cannot be determined by analytical means and numerical techniques such as the method of lines (used by Berini) and the finite element method must be used instead. Berini also showed that the field distribution along the stripe waveguide width can resemble a Gaussian field closely enough that LR-SPPs can be efficiently excited with end-fire excitation. This was realized experimentally shortly thereafter on a 8 μm wide, 20 nm thick and 3.5 mm long gold stripe embedded in SiO_2 using a polarization maintaining optical fiber at $\lambda = 1550$ nm [6].

3 Modeling

This section explains how the finite element method was used with the help of the software suite COMSOL MultiphysicsTM to model the behavior of LR-SPP waveguides and devices. The chapter starts with an introduction to the finite element method and COMSOL, and is followed by a look at the relevant partial differential equations and the corresponding boundary conditions. The different types of meshes available in COMSOL are discussed, as well as how they can be manually defined in order to mesh thin stripe waveguides. The chapter concludes by explaining how the various aspects of the finite element methods and material properties were tied together to produce realistic models of resistively heated LR-SPP waveguides.

Although most of the modeling was done in COMSOL, for the most part the discussion keeps clear of aspects that are specific to COMSOL and instead focuses on the parts of the modeling that all modern finite element software have in common.

3.1 The finite element method and COMSOL

The finite element method (FEM) is a numerical technique for finding approximate solutions to problems that can be described by partial differential equations (PDEs) or the minimization of a functional. It first originated as a method for analyzing stress in civil engineering, but has since then found its way into a number of different scientific disciplines where it has become a key technology in the modeling of advanced engineering and scientific problems, such as heat transfer, fluid flow, electric and magnetic fields and many others. The versatility of the method, along with the fact that it can be applied to problems involving complex geometries and boundaries with relative ease, has made it particularly popular in academic and commercial circles.

The basic idea behind the finite element method is to partition, or *discretize*, the geometry into smaller pieces called finite elements. Each element is of a simple geometry and thus much easier to analyze than the actual structure. The elements are connected to each other at their corners, known as vertices, and together they form a mesh of the actual structure. Within each of the elements, the unknown field quantity being sought ϕ (e.g. the temperature or electric field) is approximated with the use of simple smooth functions such

as polynomials, known as interpolation or shape functions. The field quantity can then be expressed as [22]

$$\phi = N_1\phi_1 + N_2\phi_2 + \cdots + N_m\phi_m$$

where the N_i are the interpolation functions and the ϕ_i are the values of the unknown field at the element vertices. Finite elements with linear interpolation functions produce exact values for ϕ_i if the solution being sought is quadratic, quadratic elements give exact values for ϕ_i for cubic solutions, etc [23]. The solutions are however in general not exact and the accuracy can depend highly on the number of elements used. A finer mesh will normally yield more accurate results but at a greater computational cost. For this reason the mesh is normally not uniform over the entire structure, but rather finer in regions where the rate of change of the field is great or where the precision of the result is critical to the analysis.

By applying the appropriate laws or principles, depending on the particular problem, a matrix equation governing the behavior of each element can be obtained. This resulting element characteristic matrix has different names depending on the particular field of study: in solid mechanics it is called the *stiffness* matrix and in heat conduction it is called the *conductivity* matrix. There are several ways of deriving the element characteristic matrix, the most important being the variational method and the weighted residual method.

The variational method is applicable to problems that can be stated as the minimization of a functional, such as a functional describing the total energy of the system (cf. Hamilton's principle). The variational approach can be used as long as a variational principle corresponding to the problem of interest exists, but this is not always the case. The weighted residual methods are particularly suited for problems for which differential equations are known but no variational statement is available [24]. They are based on the minimization of the residual left after an approximate or trial solution is substituted into the differential equations governing the problem [22], and are general mathematical tools applicable, in principle, for solving all kinds of partial differential equations [25]. The most popular variational method is the so-called Galerkin method [24].

Once all the element characteristic matrices have been established, they are assembled into a global set of linear simultaneous equations for the entire problem domain, which can be easily solved to obtain the required field quantity at the vertices, ϕ_i . The assembly is performed by adding up all the contributions

to a mesh vertex from each of the elements that share it. Before the global system of equations is solved, it must be modified in order to take the boundary and initial conditions into account.

The global system of equations typically involves a sparse and symmetric matrix and the problem can thus be efficiently solved with methods designed to handle such matrices, much more efficiently than say, by inverting it. There are two main types of methods for solving simultaneous equations: direct methods and iterative methods [25]. Direct methods include the well known Gauss elimination and LU decomposition methods and require that the system of equations is fully assembled before they are initiated. They can therefore require significant storage space, especially for problems involving a great number of mesh vertices. Iterative methods, such as the Gauss-Seidel method, tend to work better for larger systems since they can be coded in a way that avoids the full assembly of the system matrix [25].

The final step of a finite element simulation usually involves calculating all the secondary quantities of the problem, such as the conductive heat flux in the simulation of heat transfer, or the time-averaged power flow in the analysis of electric fields. In recent years, many commercial software products have become available that attempt to automate finite element simulations as much as possible, such as COMSOL Multiphysics [26].

COMSOL Multiphysics (previously known as FEMlab) is an interactive environment for modeling and solving scientific and engineering problems based on PDEs. It provides sophisticated tools for geometric modeling and a large materials database. It does not require a deep understanding of PDEs or numerical analysis but instead gives users access to the relevant variables through intuitive interfaces. COMSOL lets users define their own PDEs in the coefficient form, general form or in the weak form. It also provides several modules that are useful to various different fields, such as the acoustics module, the heat transfer module, RF module, chemical engineering module and many more. Through the Multiphysics feature, the differential equations from each of these modules can be coupled together to better describe realistic physical phenomena. Since the work presented in this thesis is concerned with the optical modes of stripe and nanowire waveguides and how waveguides can be heated to realize active devices, the simulations only make use of the heat transfer module and the RF module, and the following discussion is therefore limited to them.

The first step in creating any model in COMSOL is to define the geometry of the system with the use of a set of traditional computer aided design (CAD) tools. Next, the necessary material information such as the refractive index or thermal conductivity is provided and COMSOL provides a substantial material database to aid in this regard. COMSOL not only allows for the input of fixed material constants but also for expressions that can depend on one or more of the model's dependent variables. After the appropriate boundary conditions have been applied, the structure is discretized with one of the several meshing algorithms available and the relevant differential equation then solved.

3.2 PDEs and boundary conditions

When investigating the optical modes of metal waveguides and how they can be affected by heating, the relevant partial differential equations that must be solved are of course the heat transfer equation and Maxwell's equations. Each of these equations is associated with a set of boundary conditions.

3.2.1 Heat transfer

In order to calculate the temperature profile of a heated waveguide structure, COMSOL solves the following form of the heat transfer equation [27]

$$\rho C_p \frac{\partial T}{\partial t} + \nabla \cdot (-k \nabla T) = Q - \rho C_p \mathbf{u} \cdot \nabla T \quad (3.1)$$

where ρ is the density, C_p is the specific heat capacity at constant pressure, T is the absolute temperature, k is the thermal conductivity, Q is the power density of heat source and u is the velocity field vector of the material (only non-zero for fluids). At the boundaries of each subdomain, COMSOL offers a choice between the following boundary conditions: heat flux, thermal insulation, convective flux and fixed temperature.

The heat flux condition is a mixed boundary condition that not only accounts for general heat flux but also for transfer of heat due to convection and radiation:

$$\mathbf{n} \cdot (k \nabla T) = q_0 + h (T_{\text{inf}} - T) + \sigma \epsilon (T_{\text{amb}}^4 - T^4) \quad (3.2)$$

where \mathbf{n} is a normal vector to the boundary, q_0 represents the inward heat flux normal to the boundary from an external source, h is the heat transfer coefficient, T_{inf} is the external bulk temperature, σ is the Stefan-Boltzmann constant, ϵ the surface emissivity of the object and T_{amb} is ambient tempera-

ture.

The thermal insulation boundary condition is a special case of the heat flux condition where all the heat transfer mechanisms across the boundary have been disabled [27]

$$\mathbf{n} \cdot (k \nabla T) = 0 \quad (3.3)$$

This equation tells us that the normal component of the temperature gradient is zero, which means that there is no transfer of heat across it and the boundary is therefore insulating. The convective flux boundary condition is also a special case of the general heat flux condition, in which all the heat that passes through a boundary does so by means of convection:

$$\mathbf{n} \cdot (k \nabla T) = 0 \quad \text{where} \quad \mathbf{n} \cdot \mathbf{q} = \rho C_p \mathbf{u} T \quad (3.4)$$

where \mathbf{q} is the heat flux vector. Last but not least is the fixed temperature boundary condition which, as the name suggests, simply fixes the temperature of a boundary to a given temperature T_0

$$T = T_0 \quad (3.5)$$

3.2.2 Eigenmode analysis

The 'perpendicular waves' application mode in COMSOL is a 2D eigenmode solver which calculates the mode field $F(x, y)$ of a wave propagating in the z direction. It belongs to the RF module and solves the following version of Maxwell's curl equations for non-magnetic materials

$$\nabla \times \nabla \times \mathbf{E} - \tilde{n}^2(x, y) k_0^2 \mathbf{E} = 0 \quad (3.6)$$

$$\nabla \times \tilde{n}^{-2}(x, y) \nabla \times \mathbf{H} - k_0^2 \mathbf{H} = 0 \quad (3.7)$$

where $\mathbf{H} = \mathbf{H}(x, y) e^{i(\beta z - \omega t)}$, $\mathbf{E} = \mathbf{E}(x, y) e^{i(\beta z - \omega t)}$, $k_0^2 = \omega^2 \mu_0 \epsilon_0$ and β is the propagation constant in the z direction. In addition to the boundary conditions that always have to be satisfied in electromagnetic theory (such as the tangential component of the \mathbf{E} and \mathbf{H} fields being continuous across an interface, etc), COMSOL's RF module provides several additional types of boundary conditions designed to simplify the modeling process. These include conditions that allow the boundaries to behave as perfect electric or magnetic conductors (i.e. $\mathbf{n} \times \mathbf{E} = \mathbf{0}$, or $\mathbf{n} \times \mathbf{H} = \mathbf{0}$), and the perfectly matched layer (PML) condition. A PML is strictly speaking not a boundary condition but an additional domain that absorbs the incident radiation without producing reflections [27]. Two

further conditions are the scattering and impedance boundary conditions, and are closely related to the PML condition. The most commonly used boundary conditions in the work presented here are the perfect electrical conductor and PML conditions.

3.3 Meshing

The most delicate aspect of the simulation process is arguably the meshing of the structure. As explained before, it is not the geometry of the structure itself that gets used in the solution of the PDEs but rather the discretization, or the mesh, of the structure. A good mesh must strike a balance between being fine enough to resolve all the important aspects of the solution in enough detail, but still not consist of so many vertices that the computer's resources run out during the simulation process. Most finite element analysis software suits such as COMSOL provide automatic meshers which usually do a very good job. But because of the extreme aspect ratio of plasmonic stripe waveguides (several nm in thickness versus several μm in width) the automatic meshers are in many cases not sufficient since they often neglect to create mesh vertices inside the stripes. The user must therefore have some degree of control over how the mesh is generated. Furthermore, the mesh must reflect the fact that LR-SPP modes typically extend several μm into the cladding away from the metal waveguides. The most common types of meshes are the free mesh and mapped mesh, which consist of triangular and quadrilateral elements in two dimensional structures, respectively, and tetrahedral and hexahedral elements in three dimensions.

The free mesh is based on the Delauney algorithm which is a triangulation method valid for any number of dimensions [28]. The main strength of this method is that it can be used for all types of geometries, regardless of their shape or topology. In COMSOL, the user can influence the mesh through a set of adjustable parameters, such as by specifying the maximum element size and the element growth rate (i.e. how fast the element size may grow from an area with small elements to an area with larger ones).

The mapped mesh is substantially more limited than the free mesh and can only be used to mesh geometries that are fairly regular and rectangular. It furthermore requires that the subdomains of the geometry are free of isolated vertices and boundary segments and that they are bounded by at least four boundary segments. However, if some of these requirements are not met, the geometry can often be altered slightly in order to successfully mesh it.

COMSOL generates mapped meshes by using a mapping algorithm to define a regular grid on a unit square and then maps it onto the geometry in question using transfinite interpolation [27]. Unlike the free mesh, the generation of the mapped mesh cannot be influenced by a set of adjustable parameters. Examples of both types of meshes are shown in figure 3.1.

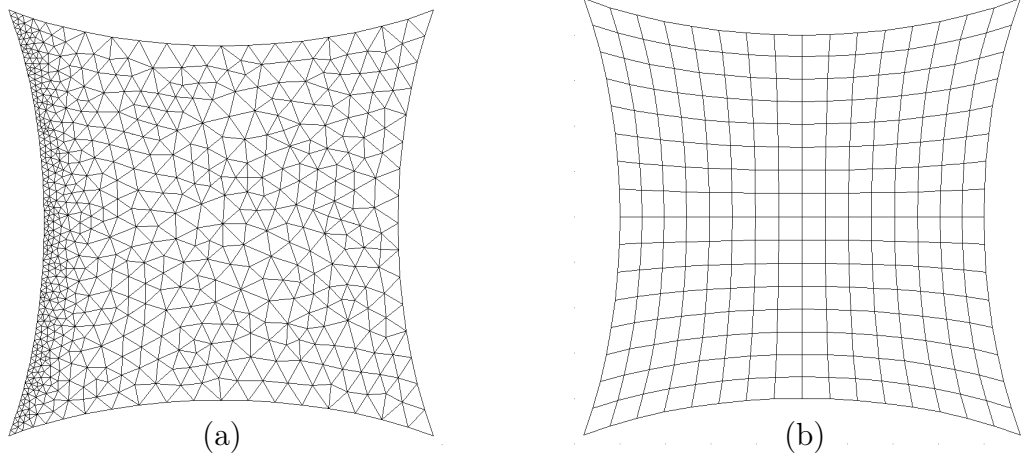


Figure 3.1: (a) A triangular mesh, where the number of edge elements has been increased on the left side in order to make the mesh denser. (b) A quadrilateral mesh of the same structure.

For both the free and mapped mesh, the boundaries of a particular subdomain can be manually partitioned into elements by specifying the number of elements and the distribution of edge vertices. This constraint forces the vertices of the subdomain mesh elements into these specified points and thus gives the user greater control over the meshing process. Figure 3.1a shows an example of such a mesh, in which the number of elements along the left edge has been fixed to 70, making the mesh much finer in this region. This feature is particularly handy when modeling plasmonic stripe waveguides since an arbitrary number of mesh vertices can be placed within the stripe, whereas the automatic meshers usually fail to insert any vertex. In much of the work presented in this thesis, the dependence of the long-range plasmon modes on waveguide geometry was investigated. By manually defining the mesh to be of a fixed density within the waveguide a degree of consistency between the models was introduced, making a comparison of the results of one geometry with another more credible. Figure 3.2 shows a typical mesh of a stripe waveguide structure, where the mesh within the metal stripe has been defined to have a fixed vertex spacing of 10 nm in the lateral direction and 1 nm in the transverse direction.

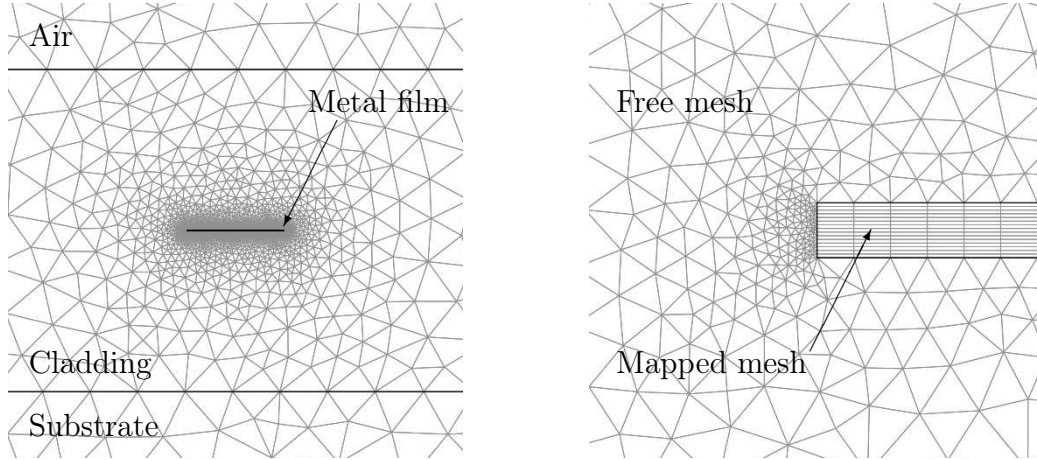


Figure 3.2: Left: The meshed geometry of a stripe waveguide, consisting of a dielectric cladding, a substrate and a thin metal stripe waveguide. Right: The details of a manually defined mapped mesh within the metal stripe, surrounded by a free mesh in the cladding region. In this case, the thickness of the metal layer is 13 nm.

3.4 Application to heated plasmonic waveguides

3.4.1 Temperature dependent material properties

As discussed in section 3.2, the eigenmode analysis and the calculation of heat transfer requires the knowledge of certain material parameters, such as the thermal conductivity and refractive index. In order to accurately simulate the behavior of heated plasmonic waveguides, the models must take into account the temperature dependence of these parameters.

The waveguides investigated in this thesis consisted of gold stripes or nanowires embedded in a layer of the polymer BCB, which was supported by a silicon substrate and had its top surface exposed to air. Polymers are essential to the operation of active LR-SPP devices because of their negative thermo-optic coefficient ($dn/dT < 0$) which causes the light to be more easily coupled to freely propagating modes in the cladding when the waveguide is heated, as we shall see later. This is not the case for other dielectrics which have positive thermo-optic coefficients, such as glass.

As explained before, in COMSOL the material properties may be specified as temperature dependent expressions instead of only constants. Therefore,

for the three materials: air, gold and BCB, experimental data on the temperature dependence of the thermal conductivity k , the heat capacity C_p and the density ρ was fitted in order to obtain such expressions. Figures 3.3 through 3.5 show the fitted datasets.

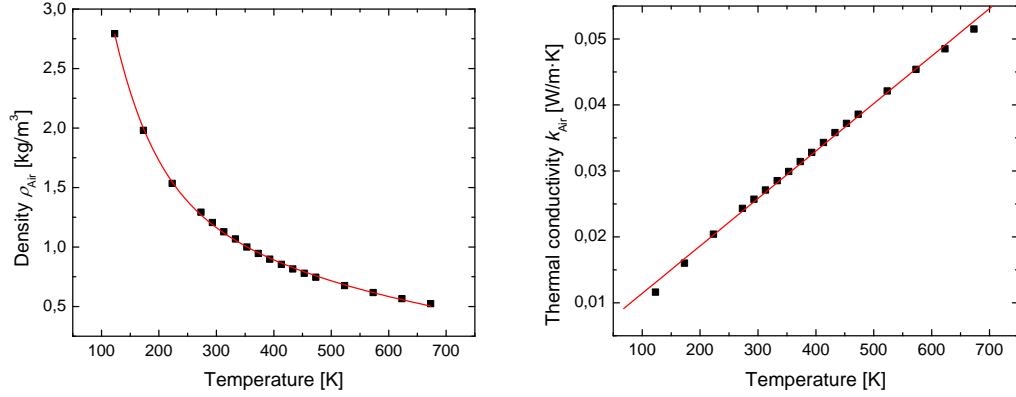


Figure 3.3: The density ρ_{Air} (left) and thermal conductivity k_{Air} (right) of air as a function of temperature. The data is from ref. [29].

For air, the following temperature dependent expressions for the density and thermal conductivity were obtained:

$$\begin{aligned}\rho_{\text{Air}} &= 7.24e^{-1.4 \cdot 10^{-2}T} + 1.91e^{-2 \cdot 10^{-3}T} \text{ kg/m}^3 \\ k_{\text{Air}} &= 7.2 \cdot 10^{-5}T + 4.2 \cdot 10^{-3} \text{ W/(m} \cdot \text{K)}\end{aligned}$$

The heat capacity of air was found to vary only by about 2% in the temperature range 300-400K, with an average value of $C_p^{\text{Air}} = 1.05 \text{ kJ/(kg}\cdot\text{K)}$. The temperature dependence of C_p^{Air} was therefore ignored in the simulations. The same applies to the temperature dependence of the densities of gold and BCB, which also do not vary much in this temperature range. Figure 3.4 shows the fitted experimental data for gold.

The corresponding fitted expressions were obtained:

$$\begin{aligned}k_{\text{Au}} &= -6.4 \cdot 10^{-2}T + 336.4 \text{ W/(m} \cdot \text{K)} \\ C_{p\text{Au}} &= -3.5 \cdot 10^{-7}T^3 + 5.4 \cdot 10^{-4}T^2 - 0.24T + 162.34 \text{ J/(kg} \cdot \text{K)}\end{aligned}$$

Unfortunately, the only temperature dependent data supplied for BCB by its manufacturer is the thermal conductivity, which is shown in figure 3.5. The

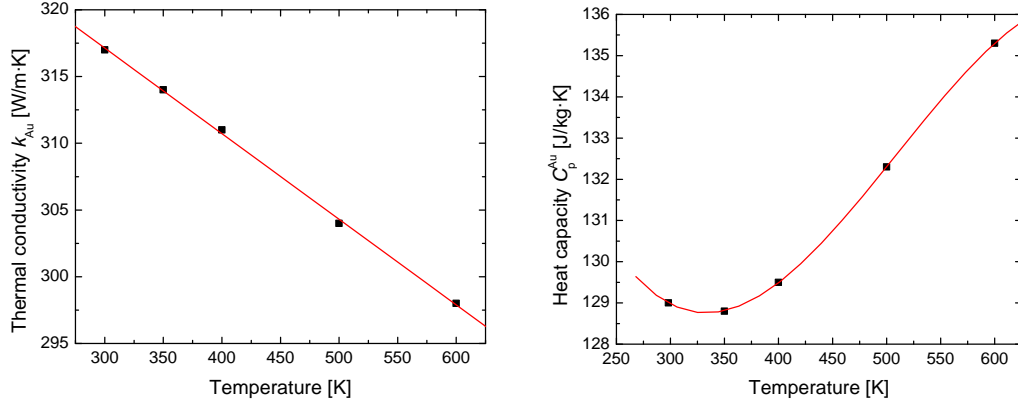


Figure 3.4: The thermal conductivity k_{Au} (left) and heat capacity C_p^{Au} (right) of gold as a function of temperature. The data is from ref. [30] and [31].

corresponding fitted expression is

$$k_{BCB} = 7.38 \cdot 10^{-4}T + 7.42 \cdot 10^{-2} \text{ W}/(\text{m} \cdot \text{K})$$

According to ref. [32], the remaining parameters are $\rho_{BCB} = 1050 \text{ kg/m}^3$ and $C_p^{BCB} = 2180 \text{ J}/(\text{kg} \cdot \text{K})$ at room temperature. The heat capacity of other polymers such as PMMA increases as much as 40% in the temperature range 300-380 K [33], i.e. from room temperature up to the materials glass transition temperature. Since the plasmonic waveguides are mostly made of BCB,

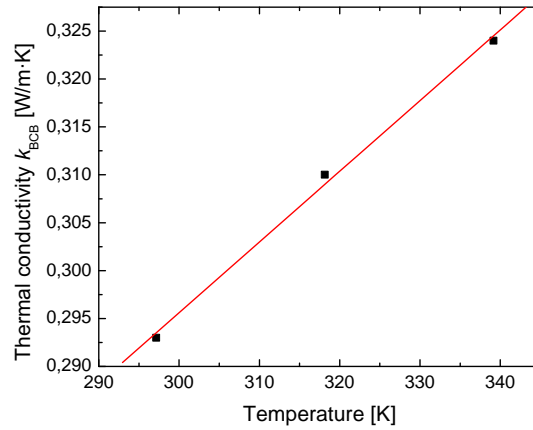


Figure 3.5: The thermal conductivity of BCB k_{BCB} as a function of temperature T . The data is from ref. [13].

a more accurate description of their heating would be obtained by relying on experimentally observed data of the heat capacity versus temperature instead just of a constant value. Unfortunately, this is unavailable at present and the models must make do without it.

The optical properties of the BCB and gold are also temperature dependent. The thermo-optic coefficient of BCB has previously been determined to be $dn/dT \sim -2.5 \cdot 10^{-5} \text{ K}^{-1}$ [34], and assuming that dn/dT is itself not temperature dependent, the relation between n_{BCB} and T can be written as

$$n_{\text{BCB}}(T) = -2.5 \cdot 10^{-5}T + C \quad (3.8)$$

where C is a constant. In order to determine it, we must know the refractive index of BCB at a given temperature. Figure 3.6 shows the wavelength dependence of n_{BCB} at room temperature.

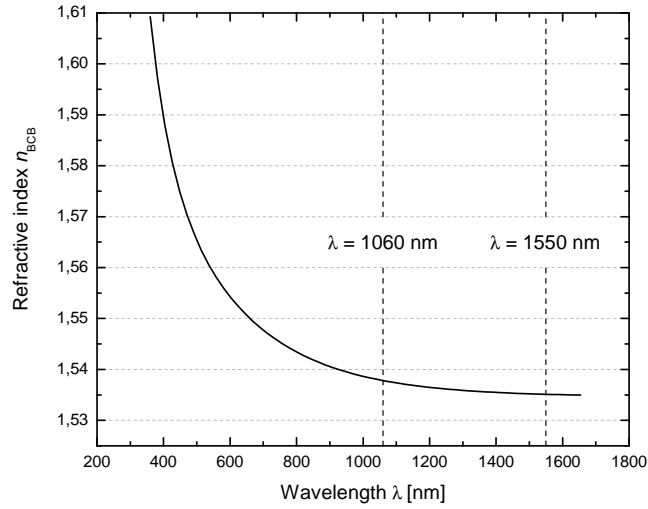


Figure 3.6: The refractive index of BCB as a function of wavelength after curing at 250°C for 60 minutes. The figure is adapted from ref. [13].

In addition to the telecommunication wavelength $\lambda = 1550 \text{ nm}$, the shorter wavelength $\lambda = 1064 \text{ nm}$ is also of interest due to the availability of laser sources operating at this wavelength and the fact that it can be detected by cheap CCD cameras. From figure 3.6 we can see that the refractive index of

BCB at room temperature is $n_{\text{BCB}} = 1.538$ for $\lambda = 1064$ nm, and $n_{\text{BCB}} = 1.535$ for $\lambda = 1550$ nm, which leads us to the following temperature dependent expression for n_{BCB}

$$n_{\text{BCB}}(T) = \begin{cases} -2.5 \cdot 10^{-5}T + 1.5425 & \text{for } \lambda = 1550 \text{ nm} \\ -2.5 \cdot 10^{-5}T + 1.5455 & \text{for } \lambda = 1064 \text{ nm} \end{cases} \quad (3.9)$$

Similarly, the temperature dependent refractive index of gold $n_{\text{Au}} = n + i\kappa$ must be determined. According to ref. [35], the thermo-optic coefficients of n and κ are

$$\begin{aligned} dn/dt &\approx 3.5 \cdot 10^{-4} \text{ K}^{-1} \\ d\kappa/dt &\approx -1.4 \cdot 10^{-3} \text{ K}^{-1} \end{aligned} \quad (3.10)$$

for $\lambda = 1064$ nm and

$$\begin{aligned} dn/dt &\approx 5 \cdot 10^{-4} \text{ K}^{-1} \\ d\kappa/dt &\approx -1.7 \cdot 10^{-3} \text{ K}^{-1} \end{aligned} \quad (3.11)$$

for $\lambda = 1550$ nm. In the latter case, the thermo-optic coefficients have been extrapolated to a wavelength of $\lambda = 1550$ nm since the data in ref. [35] only goes up to a wavelength of $\lambda = 1240$ nm. The complex refractive index of gold at room temperature at these wavelengths is (see figure 2.2)

$$\tilde{n}_{\text{Au}} = \begin{cases} 0.26 + 6.96i & \text{for } \lambda = 1064 \text{ nm} \\ 0.52 + 10.73i & \text{for } \lambda = 1550 \text{ nm} \end{cases}$$

This, in addition to the thermo-optic coefficients leads us to the following temperature dependent refractive index of gold

$$\tilde{n}_{\text{Au}}(T) = \begin{cases} (5 \cdot 10^{-4}T + 0.37) + i(-1.7 \cdot 10^{-3}T + 11.24) & \text{for } \lambda = 1550 \text{ nm} \\ (3.5 \cdot 10^{-4}T + 0.15) + i(-1.4 \cdot 10^{-3}T + 7.38) & \text{for } \lambda = 1064 \text{ nm} \end{cases} \quad (3.12)$$

3.4.2 The modeling of heated waveguides

As explained before, the first step in any finite element simulation is to specify the geometry of the structure being investigated. It is naturally neither possible nor practical to perfectly replicate the structure of the subject, and certain simplifications must therefore be made.

In simulating the plasmonic waveguides, the stripes or nanowires were positioned in the direct center of the BCB cladding, which was 20 μm thick in

the case of stripe waveguides and anywhere between 20 and 40 μm in the case of nanowires. Although the width of the BCB is in practice of the order of millimeters, it was normally limited to $\sim 100\ \mu\text{m}$ since the waveguide mode profiles were found to vanish at around 20 μm away from the stripe. Initially, a 10 μm thick silicon substrate beneath the BCB was also included in the models but was found to have a negligible effect on the calculated modes and effective mode indices. It was therefore eventually omitted to save on computing time. Last but not least, the entire structure was simulated as being enclosed by a layer of air which was thick enough so that at least one row of mesh vertices was placed in the middle of the air layer when it was automatically meshed.

The resistive heating of the waveguide structure was introduced into the models by setting the metal waveguides as heat sources of constant power. In order to increase the accuracy of the simulations the temperature dependent thermal properties and refractive index as determined in section 3.4.1 were used. The silicon substrate was assumed to act as an efficient heatsink at room temperature and a fixed temperature boundary condition was therefore applied to the lower BCB boundary, as shown in figure 3.7. Because of the fixed temperature boundary condition, the silicon substrate didn't have any influence on the resulting temperature profile and the thermal properties of silicon were therefore not needed. Furthermore, in many of the models the silicon was simply omitted, as noted before. The most natural way of modeling the effect of air at the top BCB surface would have been to apply a general heat flux boundary condition to the boundary. However, modeling with convective heat transfer can often be quite problematic because the heat transfer coefficient between air and many materials, such as BCB, is not known. Furthermore, some assumptions about the velocity field of the air have to be made which are hard to justify without having made detailed investigations on the flow of air around such a small structure. The loss of heat to the surroundings were therefore instead modelled by setting the temperature distribution to be continuous across the BCB boundary¹ and setting the outer boundaries of the air box to be fixed at room temperature. The continuity boundary condition effectively treats the air as being still, but still being able to remove heat from the structure.

Once the models had been set up in this manner, the temperature profiles were calculated using equation (3.1). Figure 3.7 shows an example of such temperature profiles, although it should be borne in mind that not all of the enclosing air is shown.

¹This arises naturally in finite element simulations due to the continuity of the finite element field.

The effect of placing an efficient thermal sink at the top interface was also investigated by setting the top BCB boundary to a fixed temperature. As can be seen from figure 3.7, this results in a more symmetric temperature profile, which is to be expected. The detailed results of these temperature simulations are presented in the following chapter.

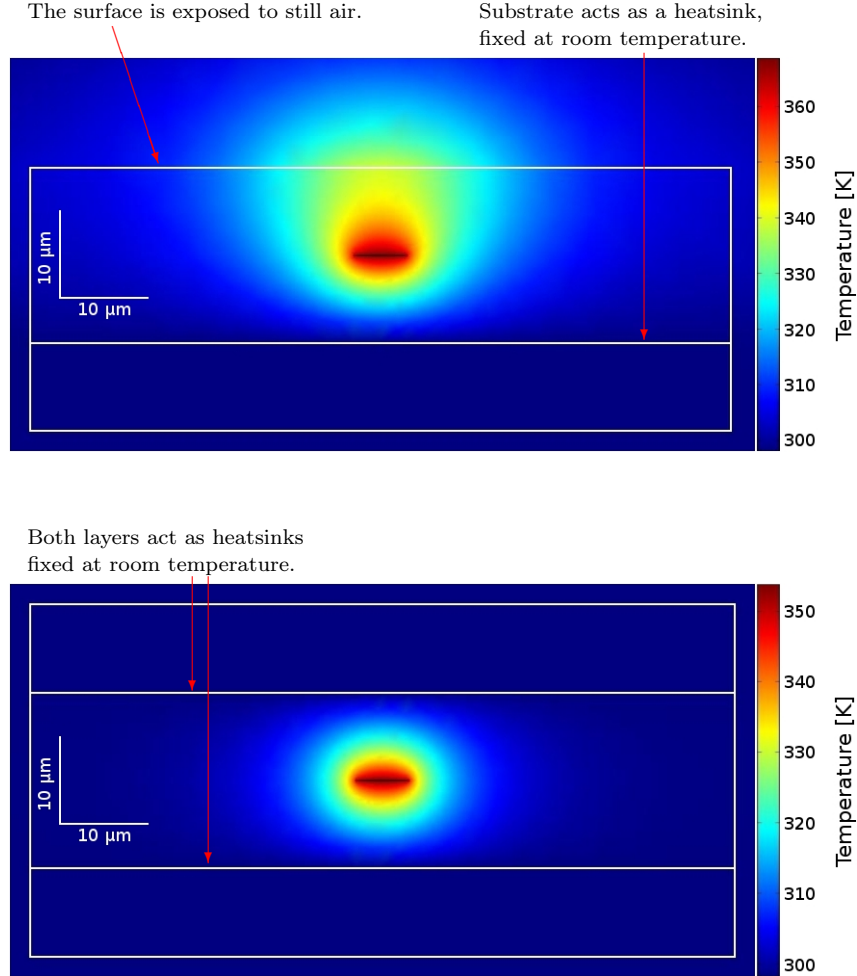


Figure 3.7: The temperature profiles of a gold stripe heated with 50 mW/mm with asymmetric (above) and symmetric cooling conditions (below).

In order to calculate the optical mode profiles and the corresponding effective mode indices, the calculated temperature profiles were used to determine the temperature dependent refractive index of both the BCB cladding and the metal waveguides using equations (3.9) and (3.12). This information was in

turn used to calculate the optical mode profiles and the effective mode indices via equations (3.6) and (3.7). COMSOL handles all the natural boundary conditions of the electric and magnetic fields automatically, but additionally the outer boundary of the air box was set to behave as a perfect electric conductor. In principle, the type of boundary condition should not matter since the field will be confined to within the BCB because of the surrounding air.

In addition to the LR-SPP modes supported by the stripes and nanowires, the cladding of a structure is also capable of sustaining a number of optical modes (known as cladding modes) due to its refractive index being higher than that of the surrounding air. Furthermore, a geometry can be found to sustain a number of different modes which are simply artifacts of the particular discretization used, the selected cladding geometry and the solution process. For these reasons, COMSOL limits the number of modes it searches for and requires the user to enter a reasonable initial “guess” of the effective mode index of the desired mode. Because the metal waveguides are so tiny compared to the cladding, the effective mode index of LR-SPP modes is usually only slightly higher than the refractive index of the cladding. Therefore, a value around 0.1% higher than the cladding index normally serves as a good initial guess. A bad initial guess can lead to vastly increased and unnecessary computing times and in the worst case scenario will cause the program to only find the unphysical modes.

4 Stripe waveguides

In this chapter, the simulations of LR-SPP stripe waveguides and LR-SPP-based active devices are presented. The chapter starts by outlining the fabrication process of stripe waveguides, and then discusses how the stripe geometry was optimized with respect to coupling to standard single mode fibers and waveguide insertion loss. It is shown that by using the metal stripes as heating elements the effective mode indices of the LR-SPP modes can be controlled, which can be used to realize active devices such as variable optical attenuators (VOAs), directional couplers and multimode interferometers.

4.1 Fabrication

The LR-SPP stripe waveguides investigated in this thesis are typically fabricated as follows: First, a silicon wafer is spin-coated with an adhesion promoter, followed by a several μm thick layer of the polymer benzocyclobutene (BCB)¹ and then soft cured in a nitrogen atmosphere. The purpose of the nitrogen environment is to prevent oxygen from diffusing into the polymer and altering the refractive index and increasing the absorption loss. Next, the wafer is spin-coated with a layer of ultraviolet photoresist and placed on a hotplate to bake out the solvent. The resist is patterned by exposing it to UV light through a mask and then submerging the wafer in a developing agent. The metal stripes are defined by thermally evaporating a nm-thick layer of gold onto the wafer and then removing the leftover resist along with the unwanted gold in a resist remover. In order to create a symmetric cladding environment, a second equally thick layer of BCB is spun onto the wafer and hardbaked in a nitrogen atmosphere. If the waveguides require electrical contacts, an analogous lithography process needs to be performed before the stripes are sealed under the BCB. In order to expose the contacts, the BCB covering them is broken off, e.g. with a scalpel. Finally, the wafer is diced into individual components. The fabrication process is illustrated in figure 4.1. Figure 4.2 shows a schematic illustration of a completed waveguide.

¹CYCLOTENE 3022-57, DOW Chemical Co.

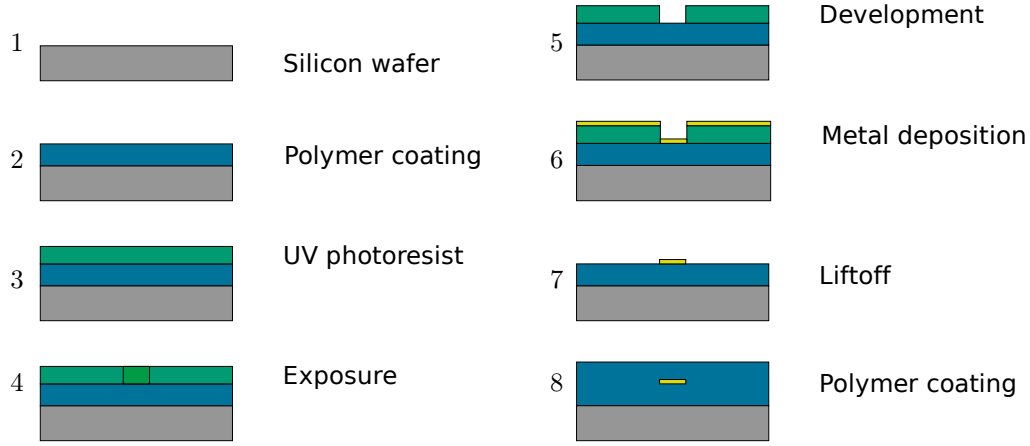


Figure 4.1: The fabrication process for LR-SPP waveguides.

4.2 Optimization

The logical place to start any investigation into LR-SPP based devices is to determine the cross-sectional geometry which minimizes the insertion loss of the device. The effective mode indices and mode fields $F_{w,t}(x, y)$ were determined in COMSOL for a range of metal film thicknesses and widths and two different free space wavelengths: $\lambda = 1064$ nm and $\lambda = 1550$ nm. The wires were embedded in the middle of a $20\text{ }\mu\text{m}$ BCB layer which was enclosed by air. The effects of the silicon substrate were neglected for the sake of simplicity since it was found to have only a slight effect on the calculated modes but led to far longer computing times. For consistency, a fixed density of mesh

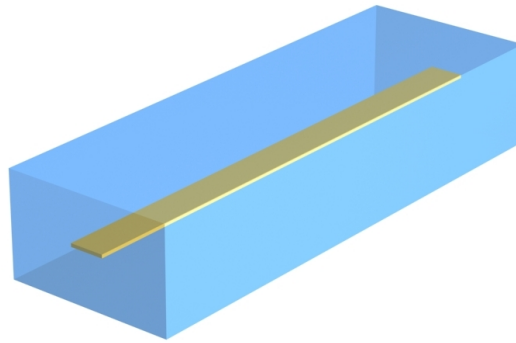


Figure 4.2: An illustration of a LR-SPP stripe waveguide embedded in a polymer.

elements in the metal stripe was used, with a 10 nm spacing in the lateral direction and a 1 nm spacing in the transverse direction. No constraints were put on the meshing in the other parts of the structure. The total number of mesh elements in the simulated area was usually of the order of $10^4 - 10^5$, which was found to give good convergence of the effective mode index. For example, increasing the number of elements from 30,000 to 140,000 in a 6 μm wide and 15 nm thick stripe only altered the real part of the effective mode index by $7 \cdot 10^{-7}$ RIU² and the imaginary part by $4 \cdot 10^{-4}$ RIU. An example of a calculated mode field $F(x, y)$ is illustrated in figure 4.3, showing the electric field intensity for a 15 nm thick and 8 μm wide gold stripe at $\lambda = 1550$ nm, along with a measured intensity profile of the same structure. The measured intensity profile was created by imaging the output of a stripe waveguide with a vidicon camera, which is sensitive to light at this wavelength.

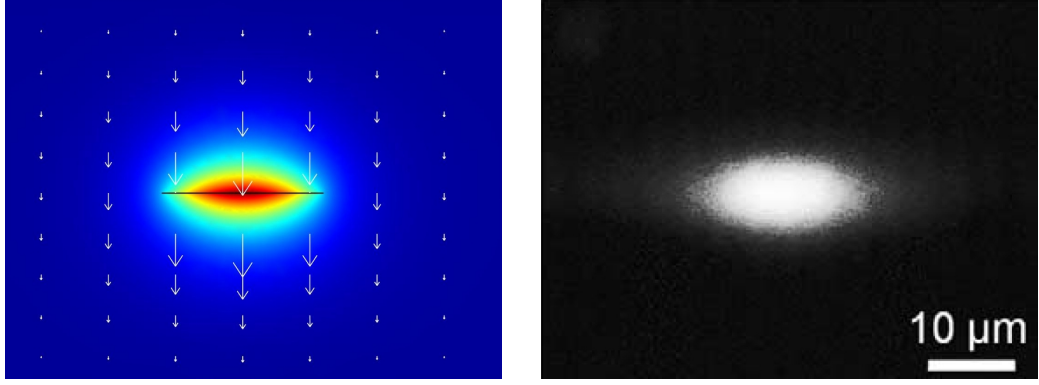


Figure 4.3: The simulated (left) and measured (right, from ref. [36]) cross-sectional intensity profiles of a LR-SPP mode excited on a 8 μm wide and 15 nm thick gold stripe at a free space wavelength of $\lambda = 1550$ nm. The arrows indicate direction and magnitude of the electric field.

For each waveguide geometry, the resulting mode profile $F(x, y)$ was used to calculate the overlap with the Gaussian fiber modes $G(x, y)$ of standard single mode optical fibers, having typical mode field diameters (MFD) of 5.4 μm in the case of $\lambda = 1064$ nm and 10.5 μm for $\lambda = 1550$ nm. Assuming that the stripe and fiber mode polarizations are in alignment, that the facet reflections can be eliminated with index-matching liquid and that good lateral and angular alignment between the stripe and fiber can be obtained, the overlap coefficient

²Refractive index units

can be calculated using

$$OL = \frac{\left[\iint F(x, y) G(x, y) dx dy \right]^2}{\iint F^2(x, y) dx dy \iint G^2(x, y) dx dy} \quad (4.1)$$

which is sufficient to estimate the loss per fiber-to-stripe coupling. The coupling loss of the various stripe geometries was obtained from

$$CL = -10 \log(OL) \quad [\text{dB}] \quad (4.2)$$

and is plotted in figure 4.4, together with the propagation loss, determined from the effective mode indices and

$$PL = \frac{40\pi}{\lambda \ln(10)} \text{Im}(n_{\text{eff}}) \quad [\text{dB/mm}] \quad (4.3)$$

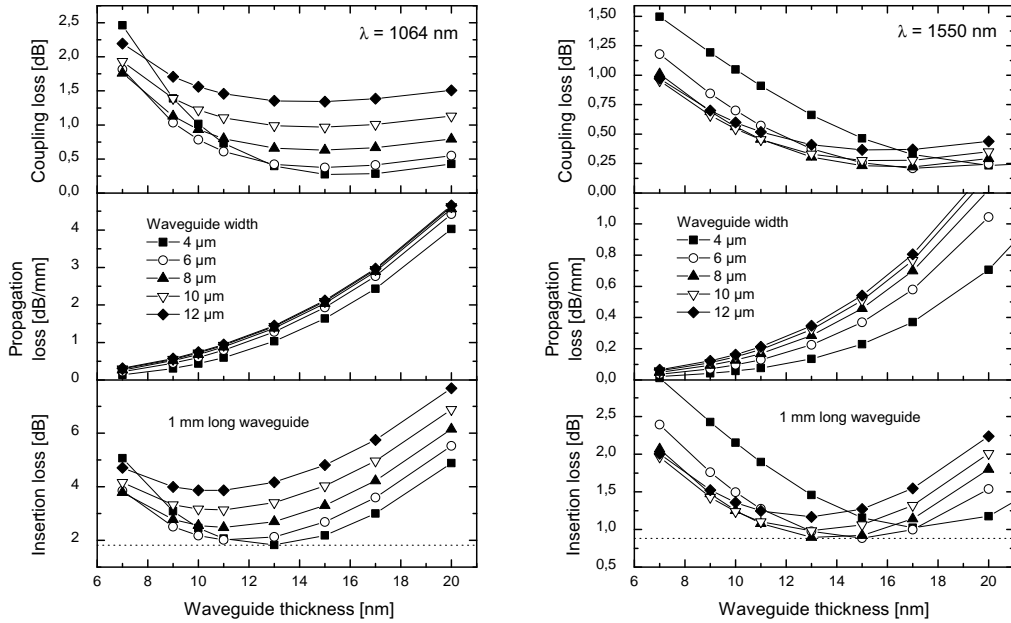


Figure 4.4: The calculated coupling loss, propagation loss and fiber-to-fiber insertion loss for 1 mm long LR-SPP gold stripe waveguides embedded in BCB at $\lambda = 1064 \text{ nm}$ (left) and $\lambda = 1550 \text{ nm}$ (right).

Despite the exponentially decaying nature of the field intensity along the y -axis, maximum mode overlaps of 94% and 95% (corresponding to coupling losses of ~ 0.2 dB) were obtained for $4\text{ }\mu\text{m} \times 15\text{ nm}$ and $6\text{ }\mu\text{m} \times 17\text{ nm}$ stripes at $\lambda = 1064\text{ nm}$ and $\lambda = 1550\text{ nm}$, respectively. However, the propagation loss increases rapidly with increasing waveguide thickness, so for devices of any appreciable length L , the total insertion loss (defined here as $IL = 2CL + PL \cdot L$) will be smaller for thinner stripes. Too low thicknesses, however, will result in a weak confinement, increased bend loss and potentially strong scattering loss from the waveguides. Assuming a device length of 1 mm, a minimum insertion loss of 1.82 dB can be obtained for a $4\text{ }\mu\text{m}$ wide and 13 nm thick waveguide in the case of $\lambda = 1064\text{ nm}$, whereas for $\lambda = 1550\text{ nm}$ a minimum insertion loss of 0.88 dB can be obtained for a $6\text{ }\mu\text{m}$ wide and 15 nm thick waveguide. It should be emphasized that in these calculations the propagation is solely due to the damping of the field inside the metal. Therefore, in order for an actual device to approach these values, the losses associated with the cladding polymer, scattering from waveguide imperfections, coupling to the substrate and facet reflections must be minimized.

The validity of the modeling was confirmed by comparing calculated data to mode profile measurements of a 2 mm long gold waveguide in BCB at a wavelength of $\lambda = 1550\text{ nm}$ (figure 4.5). In order to compare the two, the spatial resolution of the imaging system has to be taken into account. This was

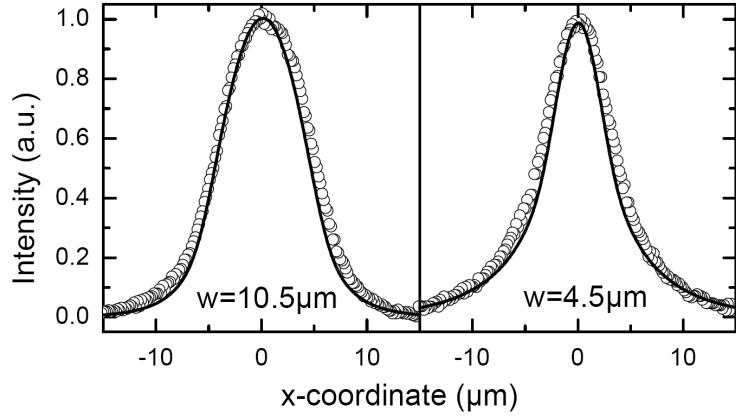


Figure 4.5: The calculated intensity profiles along the x -axis (lines) compared to measurements on a 10 nm thick, $10.5\text{ }\mu\text{m}$ and $4.5\text{ }\mu\text{m}$ wide waveguide (circles). The calculated intensity profiles were modified to take into account the resolution of the imaging optics (0.3 NA).

done by performing a 2D-convolution of the calculated intensity distribution with a response function corresponding to the spatial resolution of the imaging system, given by $1.21\lambda/\text{NA}$. Horizontal mode profiles were then obtained by integrating the resulting intensity distribution along the y -axis. As we can see, the model agrees exceptionally well with the measured data.

4.3 Heat transfer calculations

As noted before, the main advantage of LR-SPP waveguides over conventional optical fibers is their unique ability to be used simultaneously as waveguides and heating elements, which makes them ideal for realizing active devices. A good understanding of the heat transfer in LR-SPP waveguides devices is therefore required. Using COMSOL, temperature profiles were calculated for different power levels and sample geometries, using the metal stripes as a heat source of constant power. In particular, sample configurations with or without a second silicon layer in contact with the top BCB surface were investigated. In both cases, the silicon was assumed to act as an efficient heat sink fixed at room temperature. In the asymmetric case, the top BCB surface was assumed to be exposed to still air (no convective flow). Figure 3.7 shows typical temperature profiles for a 20 μm thick BCB cladding layer. In this case, the gold stripe was 6 μm wide and 15 nm thick with a heat dissipation of 50 mW/mm. Figure 4.6 shows the corresponding cross-sectional profiles for the light intensity and temperature along the x and y axes.

For a given power, the top heat sink reduces the stripe temperature by about 20% compared to a top surface in contact with air, but results in a more symmetric heating profile. In the symmetric setup, the overlap between the heated area and the mode profiles is good and 12 μm from the edge of the stripe (in the x -direction) the cladding temperature is only 3°C above ambient. Furthermore, at the power level used for the calculations in figure 4.6, the mode becomes leaky in the x -direction. This effect has been used previously to realized optical attenuators based on heated LR-SPP stripe waveguides, which is the subject of the following section. In the single heatsink setup, the resulting asymmetric temperature profile in the y direction leads to an asymmetry in the mode profile, as shown in figure 4.7. The asymmetry peaks well outside of the $1/e$ width of the mode, but will nevertheless lead to an increased coupling loss between the LR-SPP mode and a fiber mode.

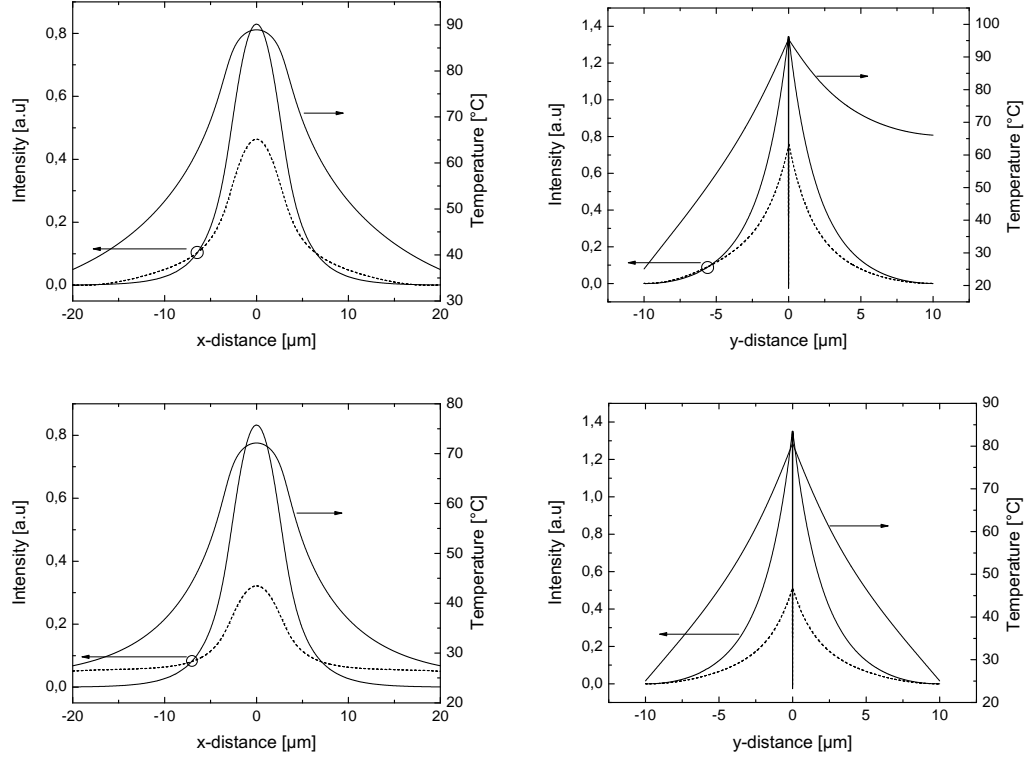


Figure 4.6: The cross-sectional temperature profiles along the x and y axes for LR-SPP waveguides with a heat dissipation of 50 mW/mm in the case of a single heatsink (above) and a double heatsink configuration (below). The intensity profiles of the LR-SPP modes are also plotted for an unheated (solid lines) and heated (dashed lines) waveguide.

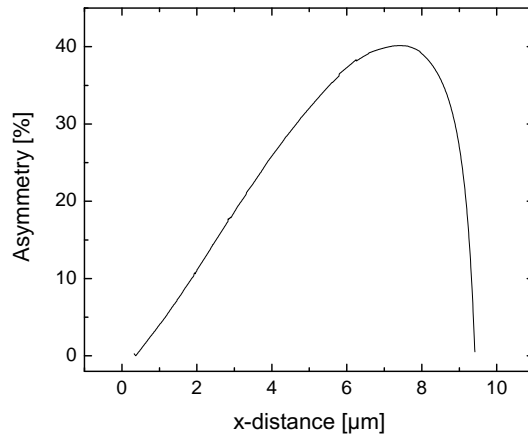


Figure 4.7: The asymmetry of the LR-SPP mode for a heat dissipation of 50 mW/mm and asymmetric cooling conditions. The asymmetry is defined as the percentage difference between the mode intensities on either side of the waveguide.

The single heatsink setup has several advantages over its double heatsink counterpart: It is easier and cheaper to fabricate, doesn't block off access to the stripe contact pads and requires lower driving currents to reach the same temperatures as in the symmetric configuration. This leads to longer waveguide lifetimes because of reduced electromigration. The asymmetric configuration is therefore used in all device simulations presented in this thesis.

4.4 Variable optical attenuators

Measurements on extinction modulators based on heated LR-SPP waveguides in a symmetric BCB cladding environment with asymmetric cooling conditions have been previously reported in the literature [36]. In this section, the mechanism of the attenuation in such a structure is studied.

Temperature profiles for a heated 6 μm wide and 15 nm thick gold stripe³ embedded in a 20 μm thick layer of BCB supported by a silicon substrate were calculated for different values of applied power. The resulting temperature profiles were then used to calculate the temperature dependent refractive index of the cladding, which in turn was used to calculate the mode fields and effective mode indices of the LR-SPP mode. Because the thermo-optic coeffi-

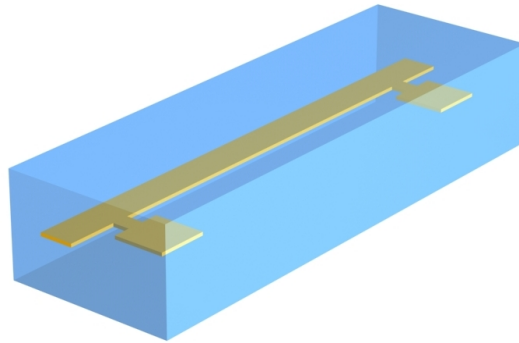


Figure 4.8: An illustration of a LR-SPP waveguide with contact pads. If a sufficiently large current is passed through the stripe it will stop guiding light, and can therefore be used as a variable optical attenuator.

³This optimal geometry for a 1 mm long waveguide at a wavelength of $\lambda = 1550$ nm, as discussed in section 4.2.

cient of BCB is negative ($dn/dT = -2.5 \cdot 10^{-5} \text{ K}^{-1}$), heating the waveguide core progressively lowers the refractive index of the surrounding cladding. This leads to a lowering of the real part of the effective mode index of the LR-SPP mode, as shown in figure 4.9. Due to the local nature of the heating however, the effective indices of cladding modes in the vicinity drop more slowly and the LR-SPP wave is thus more easily scattered into unbound modes. The light in the stripe waveguide can therefore be attenuated simply by passing a current through the stripe, which means that LR-SPP waveguides can be used as variable optical attenuators.

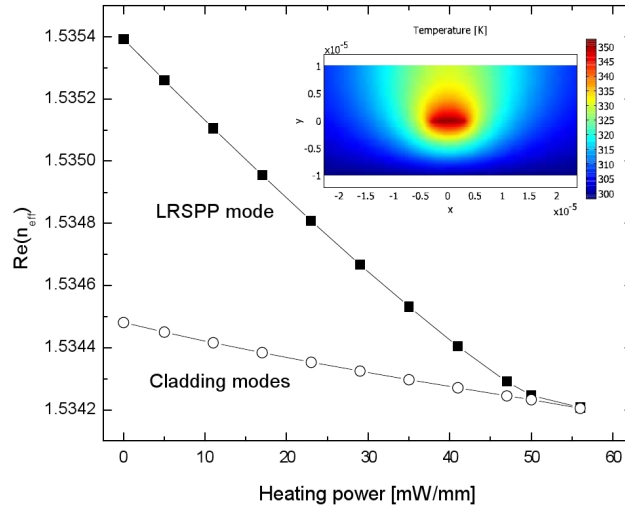


Figure 4.9: The heating of the waveguide leads to a decrease in the real part of the effective mode index of the LR-SPP mode. The temperature distribution for an applied power of 38 mW/mm, which leads to a maximum core temperature of 350K, is shown in the inset.

Figure 4.9 suggests that for an applied power of around 40-55 mW/mm, the guided wave can be efficiently coupled into the cladding layers. This is indeed confirmed by measurements of the extinction ratio of a 6 μm wide and 16 nm thick gold stripe at $\lambda = 1550 \text{ nm}$, shown in figure 4.10. The total length of the stripe was 2 mm, with a 1 mm long heated section. An extinction ratio of 45 dB is obtained for an applied power of around 50 mW/mm, which is comparable to or better than commercially available variable optical attenuators [37, 38], but with the added benefit of the stripe having a significantly smaller footprint. The observed dip at around 30 mW/mm is most likely due to destructive interference from light that has been expelled into the cladding and is traveling at a different velocity than the guided light.

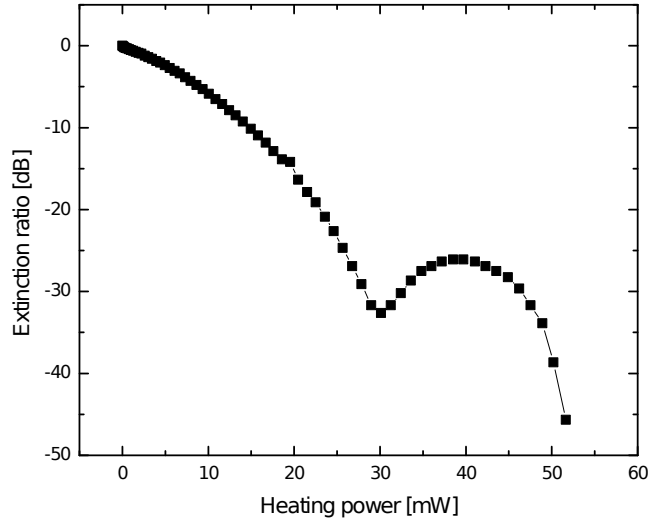


Figure 4.10: The measured extinction ratio of a variable optical attenuator made from a 6 μm wide and 16 nm thick gold stripe with a total length of 2 mm and a 1 mm heated section.

As discussed in section 4.3, the heating of the stripe waveguides leads to an asymmetry in the LR-SPP mode profile, and the coupling loss is therefore anticipated to increase with increased heating power. The coupling loss to a standard single mode fiber with a mode field diameter of 10.5 μm was therefore calculated as a function of heating power, along with the propagation loss. The results are plotted in figure 4.11 in addition to the insertion loss of a 0.1, 1, 5 and 10 mm long waveguide. As expected, increasing the heating power does indeed increase the coupling loss, and at an applied power of 40 mW/mm this behavior starts to accelerate. Conversely, due to reduced mode confinement the propagation loss decreases with increased heating power, albeit not as quickly. At power levels above 40 mW/mm, the coupling loss therefore becomes the dominant contribution to the insertion loss, which only increases by about 1.5 dB when the waveguide length is increased from 0.1 mm to 10 mm at an applied power of 50 mW/mm. The fact that the length of the waveguide plays such an insignificant role in the overall attenuation at these power levels means that compact LR-SPP variable optical attenuators with high extinction ratios but low losses can be realized, because the main drawback of plasmonic waveguides, the high propagation loss, can be sidestepped by reducing the length of the waveguide.

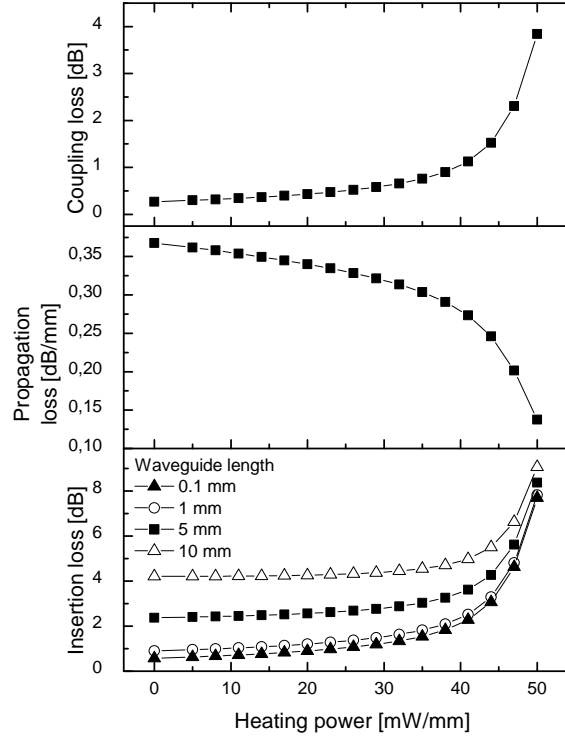


Figure 4.11: Heating the waveguide leads to increased coupling loss and insertion loss, while decreasing the propagation.

Time dependent simulations were also carried out in order to investigate the thermal response of heated waveguide structures. Figure 4.12 shows the temperature at the center of the waveguide immediately after turning on or off a 50 mW/mm heating current, along with the measured optical response of a similar device. The calculated thermal response is characterized by a 1-2 ms turn on and turn off time, which is in good agreement with the measured data and is similar to or better than that of many commercially available polymer- or MEMS-based VOAs [37, 38], although still much too slow for data transmission.

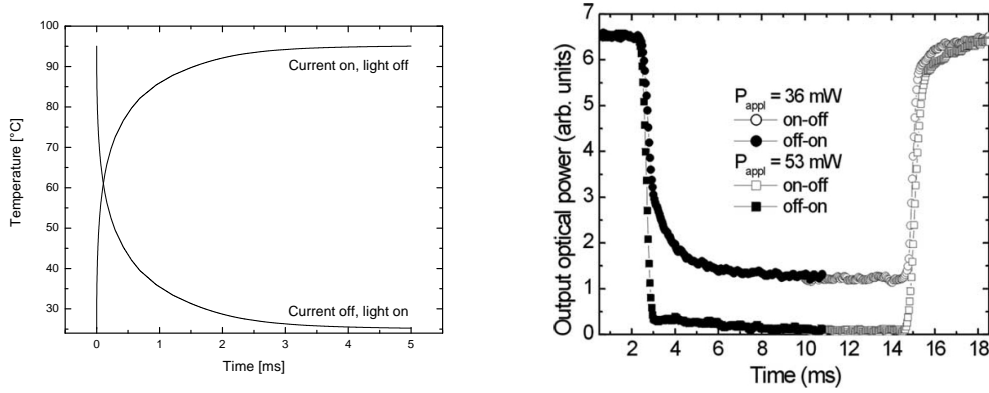


Figure 4.12: Left: The calculated temporal response of a waveguide heated with an applied power of 50 mW/mm, showing a response time of around 1-2 ms, in reasonable agreement with published experimental data (right, from ref. [36]) for a 15 nm thick, 8 μm wide and 3 mm long gold stripe in a 30 μm thick BCB cladding.

4.5 Directional couplers

The directional coupler (DC) is an important device in the field of integrated optics since it can be used to create power dividers, switches, filters and more. In its simplest form, a directional coupler consists of two parallel waveguides which are placed in close proximity to each other, as shown in figure 4.13. For small separations d , the optical energy can be completely transferred from one waveguide to the other by evanescent coupling. The distance a mode must travel for it to be fully coupled to the other waveguide is given by the so-called

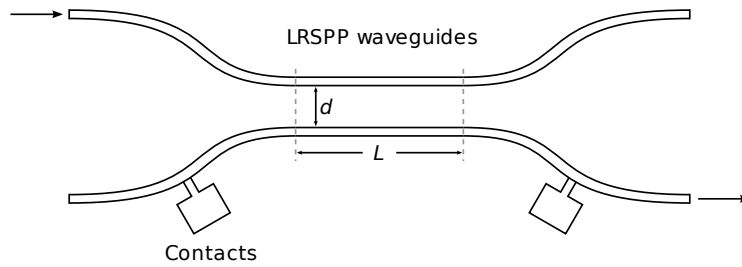


Figure 4.13: A schematic illustration of a directional coupler. In the central interaction region of length L , a guided mode can be transferred from one waveguide to the other.

coupling length [39]

$$L_c = \frac{\lambda}{2(n_{\text{eff}_1} - n_{\text{eff}_2})} \quad (4.4)$$

where λ is the free space wavelength and n_{eff_1} and n_{eff_2} are the effective mode indices of the symmetric and antisymmetric supermodes of the system, shown in figure 4.14. Because it is the evanescent mode field outside the waveguide that is responsible for the coupling, the coupling length L_c should increase with separation d . In the case when the interaction length L is an even multiple of the coupling length, the guided mode will exit the directional coupler through the same waveguide as it entered, but if L is an odd multiple of L_c it will exit through the other.

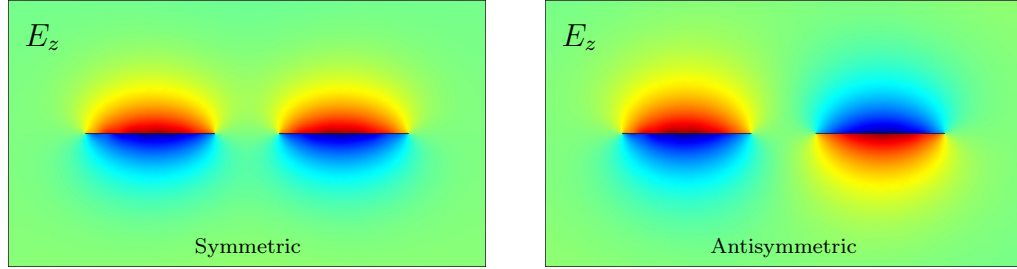


Figure 4.14: The symmetric (left) and antisymmetric (right) supermodes for two 4 μm wide and 13 nm thick gold stripes embedded in BCB, separated by 2 μm .

Directional couplers based on stripe waveguides have several interesting potential applications, since by heating one of the waveguides the coupling length can be modulated, thereby realizing optical switches, attenuators and power dividers [9].

Using COMSOL, the effective mode indices of the two supermodes were calculated as a function of waveguide separation for the wavelengths $\lambda = 1064$ nm and $\lambda = 1550$ nm. The coupling length was then obtained from equation (4.4) and plotted in figure 4.15. In both cases, the previously determined optimal waveguide geometries were used. For waveguide separations up to about 4 μm , the coupling length is quite similar for the two wavelengths, but it starts increasing much more rapidly in the case of $\lambda = 1064$ nm for longer separations. The coupling length has implications on how far apart devices must be spaced in order to avoid data transfer errors due to modes jumping from one waveguide to the next. As it turns out, parallel sections of several mm are needed for a full mode transfer, but even though only a fraction of the optical

power in a mode is lost to other waveguides, it can still lead to undesirable behavior. According to the data presented in figure 4.15, more care must be taken when designing integrated optical components operating at a wavelength of $\lambda = 1550$ nm than at $\lambda = 1064$ nm.

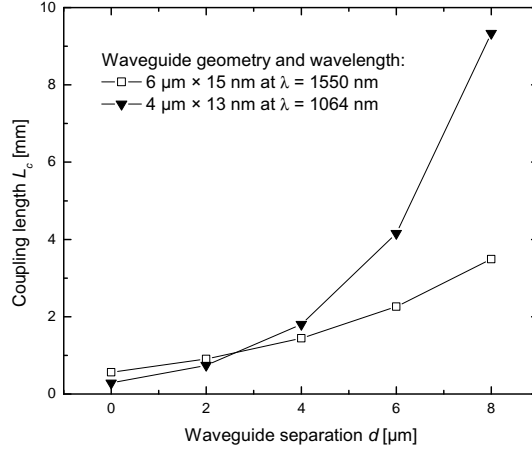


Figure 4.15: The calculated coupling length as a function of waveguide separation for two different wavelengths.

4.6 Multimode interferometers

The stripe waveguides discussed so far have only been capable of sustaining a single LR-SPP mode due to their widths being smaller than the cut-off width of the higher order modes. Figure 4.17 shows finite element simulations of the evolution of the normalized effective mode indices⁴ and propagation loss of the stripe modes as a function of waveguide width for a 15 nm thick gold stripe at $\lambda = 1550$ nm. At this wavelength and geometry, the multimode regime sets in at a stripe width of about 15 μm . In addition to more modes becoming available with increased stripe width, the propagation loss of the modes increases and approaches a constant value of around 0.6 dB/mm. In the multimode regime, the different modes supported by the stripe can interfere and cause length dependent intensity distributions. According to ref. [40], if a multimode stripe is excited by a single mode stripe placed symmetrically with

⁴Defined as the percentage difference between the effective mode index n_{eff} and the refractive index of the cladding n_{cl} : $b = (n_{\text{eff}} - n_{\text{cl}})/n_{\text{cl}}$

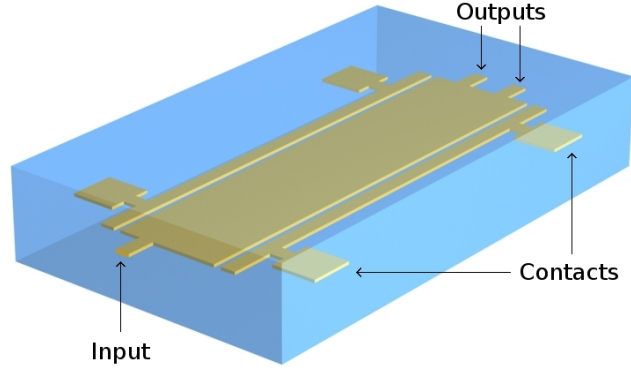


Figure 4.16: An illustration of a tunable multimode interferometer.

respect to its center line, the mode interference will lead to N -fold images at distances

$$L = \frac{3p}{8N} \frac{\lambda}{n_{\text{eff}0} - n_{\text{eff}1}} \quad \text{with } p = 0, 1, 2 \dots \quad (4.5)$$

where $n_{\text{eff}0}$ and $n_{\text{eff}1}$ are the effective mode indices of the two lowest order modes.

The goal of the present section is to show how multimode waveguides can be used to realize optical switching by using heating of the stripe edges to tune the interference pattern. Figure 4.18 show a schematic illustration of the multimode interferometer (MMI) studied. The top and bottom parts of the multimode section are electrically isolated from the central part to allow for

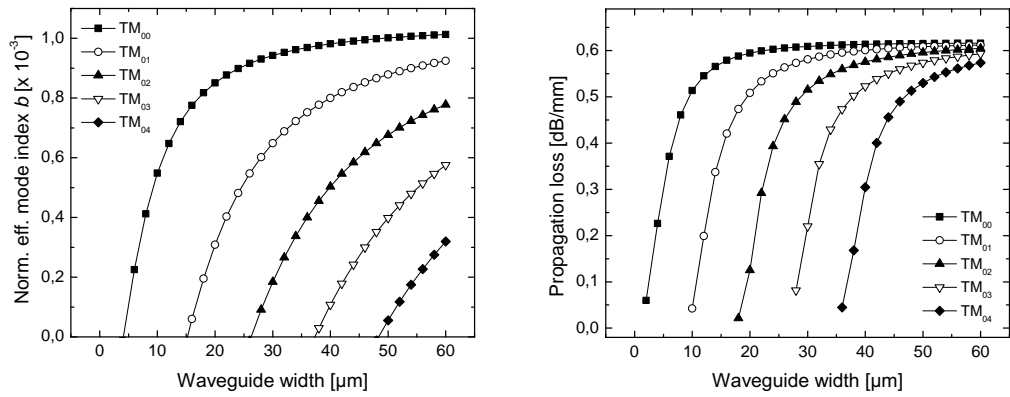


Figure 4.17: The normalized effective mode indices and propagation loss versus waveguide width for a 15 nm thick stripe at $\lambda = 1550$ nm.

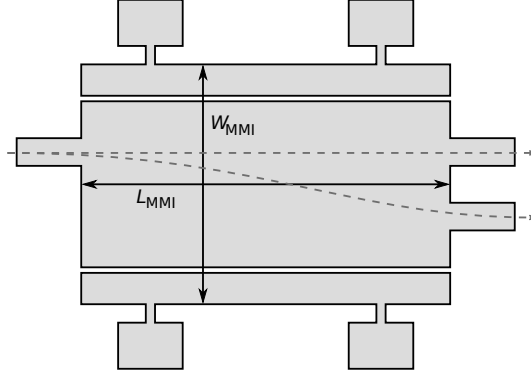


Figure 4.18: A schematic illustration of the MMI structure studied. The modes are excited asymmetrically from the off-center waveguide on the left. Reducing the refractive index at the MMI edges by passing the appropriate current through the top and bottom sections switches the light from the bottom to the top output waveguide on the right hand side.

selective heating of one or both sides of the MMI. Only the case where equal heating is applied to both edges is studied here. Because of the localization of the heating, the different modes of the multimode waveguide are affected differently, which translates to a change in the interference pattern. Figure 4.19 show finite element calculations of the modes supported by a $W_{\text{MMI}} = 40 \text{ } \mu\text{m}$ wide multimode waveguide for different heating powers, along with the corresponding effective mode indices. With increased heating, the shapes of the modes change slightly and the real part of their effective mode indices is shifted downwards. The simulations also reveal that the propagation loss of the modes increases slightly with heating, at a rate of about $5 \cdot 10^{-3} \text{ dB/mW}$.

The LR-SPP propagation in the MMI structure was simulated with FIMM-PROP, a 2D vectorial beam propagation software product from PhotonDesign [41]. The mode injected into the MMI was determined using an integrated mode solver capable of solving for thin films of complex refractive index. In order to check the validity of the propagation model a long MMI section with symmetric (centered) excitation was simulated, corresponding to devices reported in reference [8]. Good agreement was obtained with the experimentally observed 2-fold and 4-fold splitting in $40 \text{ } \mu\text{m}$ and $60 \text{ } \mu\text{m}$ wide MMI sections, respectively, confirming that the model adequately describes the LR-SPP propagation and interference, at least in the unheated case.

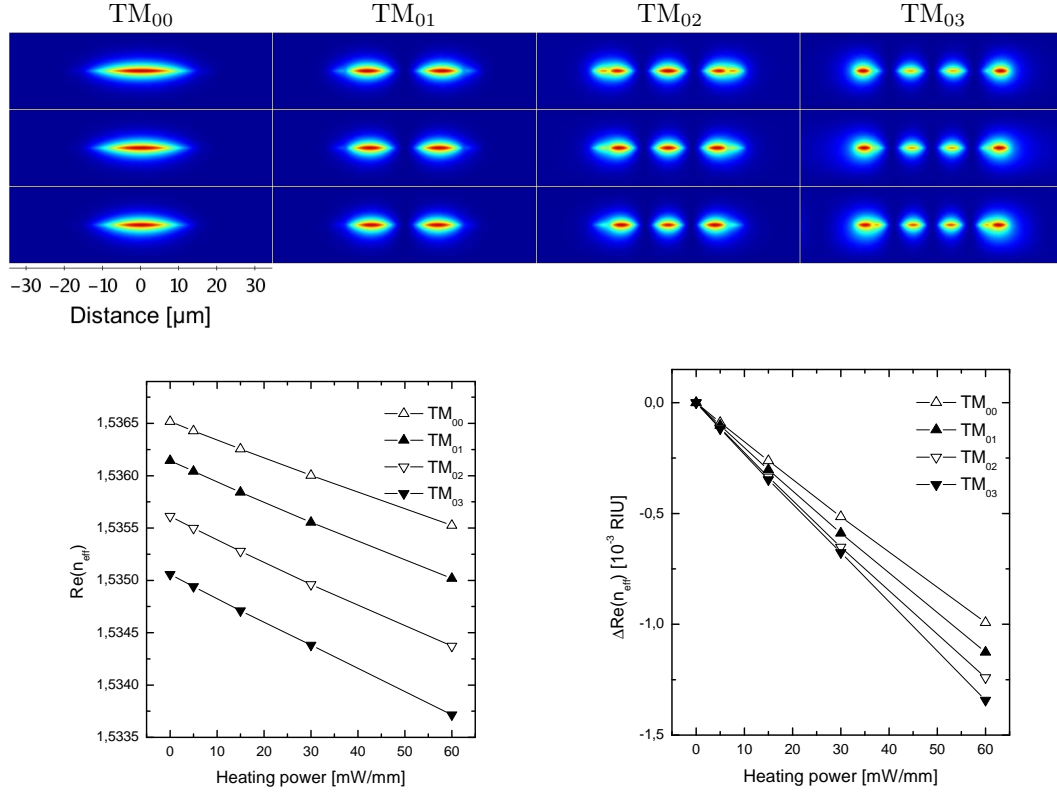


Figure 4.19: Top: The modes supported by a $W_{\text{MMI}} = 40 \mu\text{m}$ wide MMI device for no heating (top row), 30 mW/mm (middle row) and 60 mW/mm (bottom row). The width of the heated sections was $4 \mu\text{m}$ and the isolation gap was $1 \mu\text{m}$. Bottom: The effective mode indices (left) and the change in effective mode index (right) with increased heating. The change in index is more pronounced for higher order modes.

The effects of heating in the tunable MMI configuration were introduced as elliptical Gaussian variations in the refractive index of the cladding, approximately matching the temperature profiles calculated in COMSOL (see figure 4.20). The resulting effective mode indices determined by FIMMPROP differ slightly from the finite element solutions, but better correspondence can presumably be obtained by improving the description of the temperature profile. Figure 4.21 shows the intensity of the LR-SPP modes as they propagate through the $W_{\text{MMI}} = 40 \mu\text{m}$ wide and $L_{\text{MMI}} = 2.45 \text{ mm}$ long MMI section with and without an applied power of 60 mW/mm. As we can see, the effect of the heating is to switch the light from the bottom to the top output waveguide on the right. The cross-talk between the output arms was estimated to be

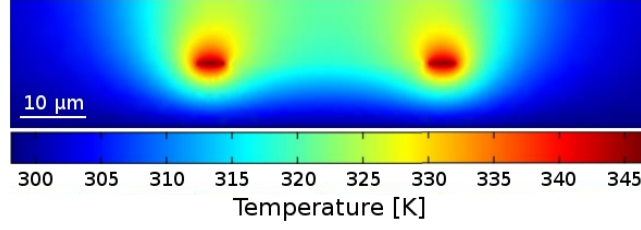


Figure 4.20: Temperature profile of the heated MMI, as determined in COM-SOL.

about -13 dB. In this case, no optimization was carried out with respect to the MMI size, the placement of the input and output waveguides or the electrode configuration in order to improve the performance of the switch. Although the design presented here is used to demonstrate 1×2 switching, it could in principle also be used to realize a 2×2 switch. There is, however, a potential problem with these MMI devices in that as the edges are heated the light in the vicinity will be more easily coupled into to the cladding which may cause the light in the MMI to be extinguished before it manages to reach one of the output waveguides. The propagation simulations did not take this into account.

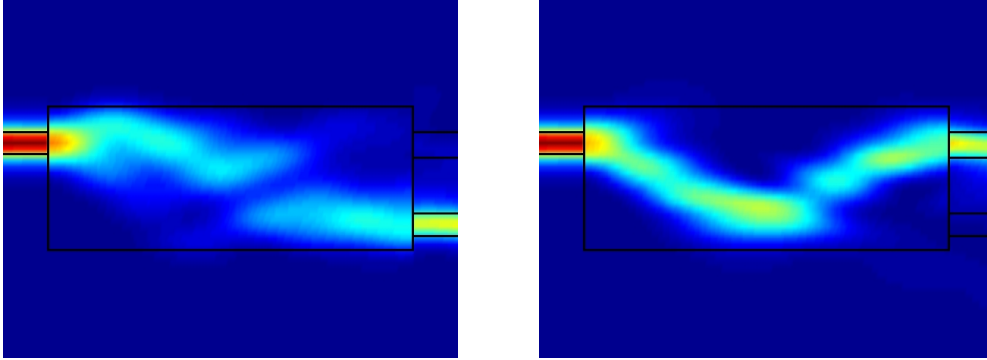


Figure 4.21: The calculated intensity of a LR-SPP mode at $\lambda = 1550$ nm propagating through a $40 \mu\text{m}$ wide and 2.45 mm long tunable MMI without heating (left) and with 60 mW/mm of heating power applied to $4 \mu\text{m}$ wide sections along the top and bottom edges of the multimode waveguide (right).

It should be kept in mind that because LR-SPP waveguides can only transmit TM polarized light, they are only useful in a limited number of cases (e.g. in laser modules). LR-SPP waveguides with square cross-sections on the other hand, have been shown to transmit arbitrarily polarized light [11, 42], and are the focus of the next chapter.

5 Nanowire waveguides

In this chapter, the properties of plasmonic waveguides based on square cross-sectional nanowires embedded in a dielectric cladding environment are investigated. As discussed below, the main advantage of such waveguides over the stripe waveguides is that they are capable of transmitting any polarization of incoming light. The chapter starts with a short introduction to square nanowire waveguides, followed by a discussion on the fabrication process. The nanowire cross-sectional geometry is then optimized with respect to coupling and insertion loss to a single mode fiber. After examining the influence of cladding thickness and waveguide asymmetry on performance the chapter concludes by investigating how waveguide heating can be used to achieve attenuation.

5.1 Introduction

As noted before, the strong polarization dependence of optical components based on stripe waveguides makes them largely incompatible with conventional fiber-optics. In order to solve this problem, Berini suggested replacing the metal stripes with metal nanowires with symmetric square cross sections [10], which were indeed experimentally confirmed to guide two orthogonal linear polarizations shortly thereafter [11].

Similarly to the short and long range modes supported by thin metal films, the supermodes supported by square nanowires are formed by mode coupling. However, instead of arising from SPPs propagating along the interfaces, the supermodes of square nanowires are formed by the coupling of plasmon polariton modes at the corners of the waveguide [12] (figure 5.1).

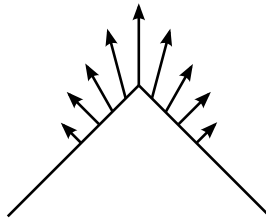


Figure 5.1: An illustration of the electric field of a fundamental plasmon mode supported by an isolated corner.

Each square nanowire is of course capable of sustaining four corner modes as well as four planar SPPs modes. For large nanowires, the corner modes do not interact and are therefore practically degenerate and all have the same effective mode index. As the nanowire sidelength is decreased and the four corner modes start to overlap, the degeneracy is lifted and new modes are formed. Due to symmetry reasons, only four new modes are allowed, which are shown in figure 5.2 along with the labeling convention introduced by ref. [12].

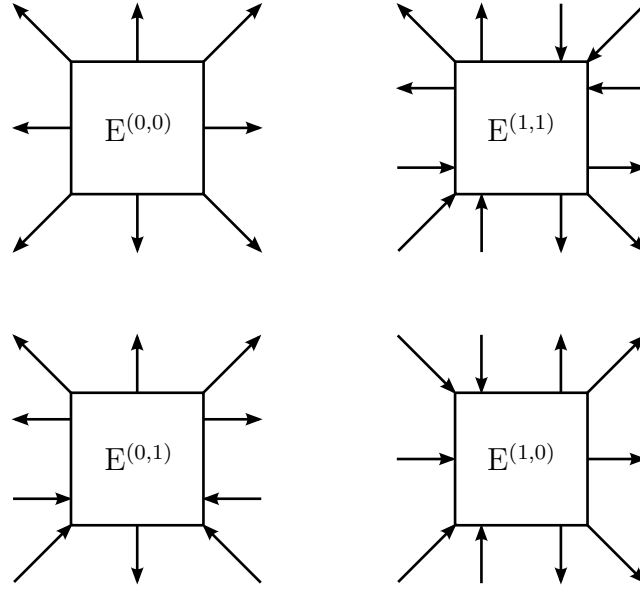


Figure 5.2: The electric field of the four supermodes arising from the coupling of corner modes.

Neither the $E^{(0,0)}$ nor $E^{(1,1)}$ modes are of much importance in waveguiding due to the short propagation distance of the $E^{(0,0)}$ mode and the fact that the $E^{(1,1)}$ mode is only supported for quite large metal core sizes, at least 1500 nm in the case of gold waveguides in BCB [12]. The $E^{(0,1)}$ and $E^{(1,0)}$ modes are however analogous to the previously discussed long range modes and can be efficiently excited by end-fire coupling from an optical fiber. Furthermore, the $E^{(1,0)}$ and $E^{(0,1)}$ modes are almost entirely polarized along the x and y -directions respectively (see figure 5.3), and since they are invariant under 90° rotation they allow for SPP guiding of any polarization of light.

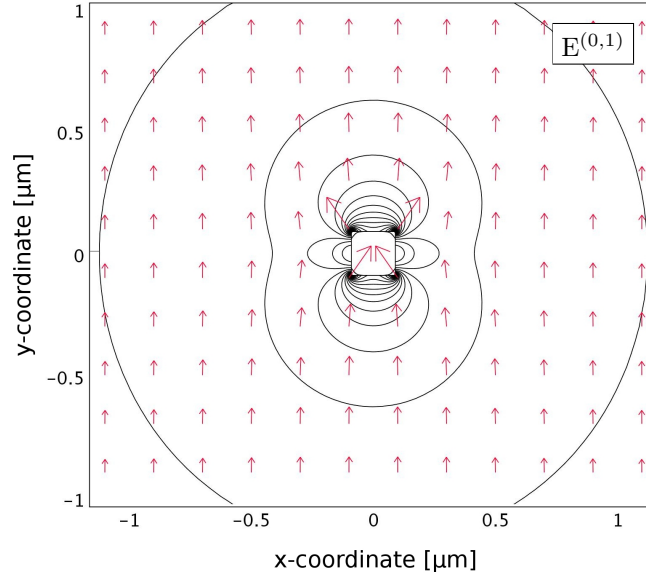


Figure 5.3: The calculated magnitude and direction of the electric field of the $E^{(0,1)}$ polarized mode in the vicinity of a 180 nm wide gold nanowire in BCB, illustrating the high field intensity close to the corners.

5.2 Fabrication

In many respects the fabrication of nanowire waveguides closely resembles the fabrication of stripe waveguides (discussed in section 4.1). The main difference lies in the fact that the nanowires require greater resolution than standard UV lithography has to offer, and therefore methods such as electron beam lithography must be used instead. As before, a silicon wafer is primed with an adhesion promoter and then spin-coated with a several μm thick layer of BCB. After curing in a nitrogen atmosphere the wafer is spin-coated with a layer of electron beam resist. In order to avoid charge build-up during the electron beam exposure, the resist is covered with a nm-thick layer of thermally evaporated aluminum. The waveguides are defined in an electron-beam writer, which is followed with the removal of the aluminum by wet-etching and the development of the resist. The gold is deposited to the desired wire thickness by electron beam evaporation and the unexposed resist then removed during a lift-off step. Next, electrical contacts are created with UV lithography following the same approach as for the fabrication of the stripes. Finally, the wafer is covered with a second equally thick layer of BCB, hard-cured in a nitrogen atmosphere and then diced into individual components.

5.3 Optimization

Proceeding as before, the effective mode indices and mode fields $F(x, y)$ were determined in COMSOL for square gold nanowires of varying side length embedded in a 20 μm thick and 80 μm wide BCB cladding bounded by air on all sides and a free space wavelength of $\lambda = 1550$ nm. In order to more accurately model the nanowires, their corners were symmetrically chamfered to a radius of 5 nm. According to ref. [12], such a modest rounding of the corners has a minimal effect on the results of the finite element calculations. Figure 5.4 shows an example of the two calculated supermodes corresponding to the $E^{(1,0)}$ and $E^{(0,1)}$ polarizations.

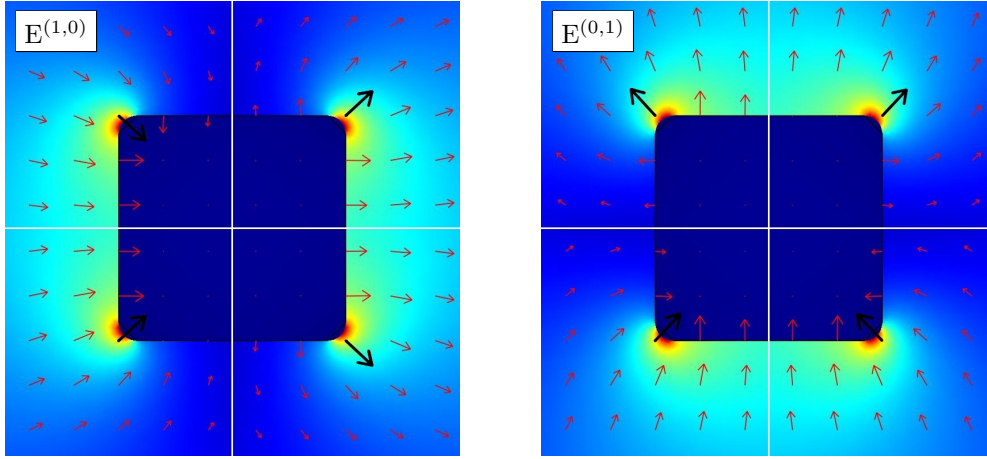


Figure 5.4: The simulated supermodes of a 150 nm wide nanowire made of gold at a wavelength of $\lambda = 1550$ nm. The central parts of the images have been removed for clarity, and the corner modes have been highlighted.

For each nanowire side length, the resulting mode profile was used to calculate the overlap with the Gaussian fiber mode of a single mode fiber with a MFD of 10.5 μm , using equation (4.1). The overlaps and the effective mode indices were then used to calculate the coupling loss and propagation loss as a function of nanowire side length via equations (4.2) and (4.3). The results are presented in figure 5.5 along with the insertion loss of a 0.5, 1 and 2 mm long waveguide components. A minimum coupling loss of 0.31 dB (corresponding to an overlap of 93%) was obtained for a 230 nm wide waveguide. Despite the asymmetric cladding environment, the results corresponding to each polarization were almost identical, and therefore only the losses of the $E^{(0,1)}$ polarization are shown.

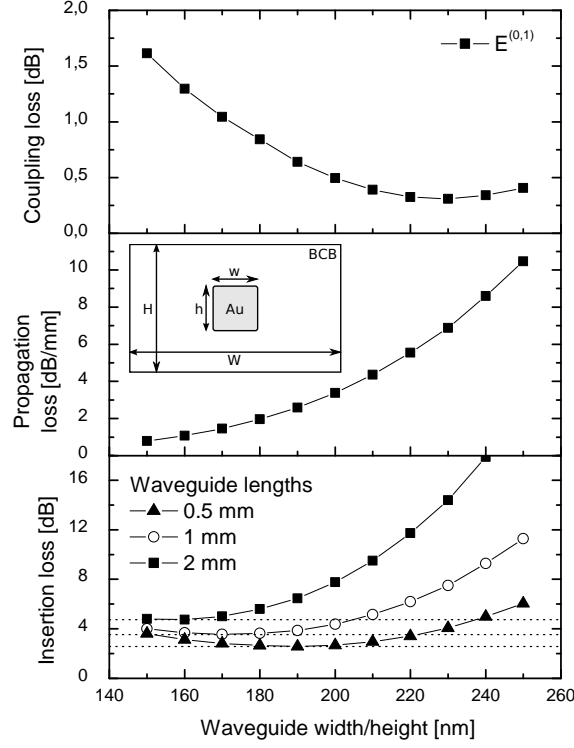


Figure 5.5: The calculated coupling loss, propagation loss and fiber-to-fiber insertion loss for 0.5, 1 and 2 mm long gold nanowire waveguides in a 20 μm thick layer of BCB at $\lambda = 1550$ nm. The calculated values were the same for both polarizations so only the $E^{(0,1)}$ results are shown.

Because the propagation loss increases monotonously with increased waveguide width, the waveguide side length that gives rise to a minimum insertion loss is shifted downwards as the device length increases: The minimum insertion loss of a 0.5 mm long device was determined to be 2.57 dB for a 190 nm wide nanowire, 3.47 dB for a 180 nm wide and 1 mm long device (which is considerably higher than the ~ 0.88 dB obtained for a 1 mm long gold stripe at the same wavelength) and 4.65 dB for a 160 nm wide and 2 mm long device. As before, the model only accounts for propagation loss due to the damping of the field in the metal and effects such as scattering losses due to imperfections in the metal are not factored in.

5.4 The influence of cladding on performance

Since the cladding layer is of a finite thickness and width, it provides additional confinement to the propagating plasmon modes, which influences both the coupling loss and propagation loss. In order to reveal how the cladding thickness influences the waveguiding abilities of square nanowires, simulations were performed for wires with sidelengths varying between 150 and 210 nm, embedded in the middle of a BCB cladding of three different thicknesses, $H = 12, 24$ and $40 \mu\text{m}$.¹ The results are presented in figure 5.6.

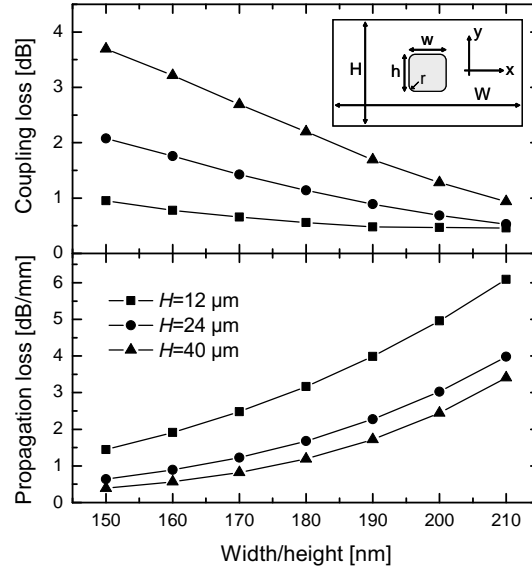


Figure 5.6: The coupling loss and propagation loss in symmetric nanowire waveguides for three different cladding thicknesses. Only the results for $E^{(0,1)}$ polarized long-range mode are shown.

As before, the coupling loss decreases with nanowire sidelength as the overlap with the fiber mode improves, whereas the propagation loss increases due to greater confinement of the mode. For narrow wires, the increased confinement from a thinner cladding substantially decreases the coupling loss while causing only a modest increase in propagation loss for short devices. In order to

¹This work and the following investigation into the influence of waveguide asymmetry on performance was done in collaboration with T. Rosenzweig and is pending publication.

minimize the insertion loss for a given device length, a compromise between the two must therefore be reached, depending on the geometry in question.

The insertion loss of three $180 \text{ nm} \times 180 \text{ nm}$ waveguides of different lengths was calculated as a function of cladding thickness, presented in figure 5.7a. For short waveguide devices lengths (0.5-1 mm), a minimum insertion loss is obtained for a cladding thickness of $H = 16 \text{ }\mu\text{m}$. Using this thickness, the effect of reducing the width of the cladding layer was also calculated (figure 5.7b). This results in a minimum insertion loss close to 1.4 dB for the 0.5 mm long device, which is substantially lower than the 2.57 dB loss obtained for an unoptimized cladding.

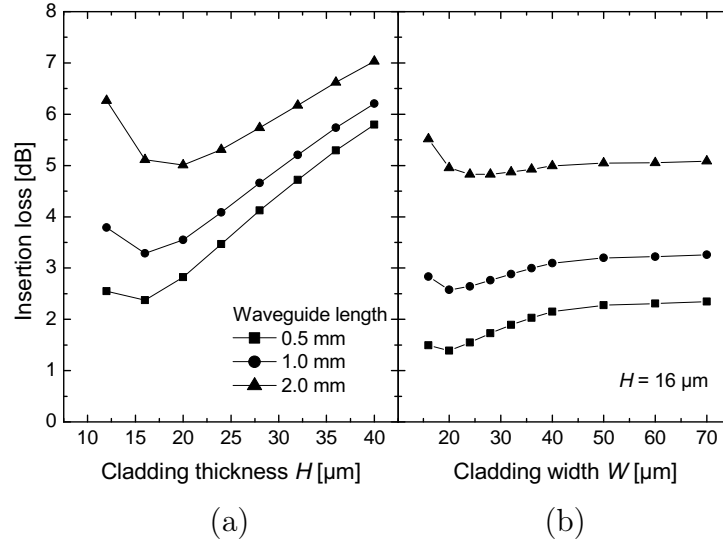


Figure 5.7: The total insertion loss for different lengths of symmetric nanowire waveguides ($180 \text{ nm} \times 180 \text{ nm}$) when the extent of the dielectric cladding layer is limited vertically (a) and both vertically and horizontally (b).

5.5 The influence of asymmetry on performance

Because of the finite resolution of the lithography methods used to fabricate the nanowires they seldom have perfectly square cross-sections. In most cases, there is a slight mismatch between the width and the height of the nanowires, and in some cases they are subject to trapezoidal deformation where the bottom of the wire is slightly wider than the top. This deviation from perfect

symmetry will result in polarization dependent loss (PDL) of the nanowires and in order for them to be a practical alternative to other methods of guiding and manipulating light, the PDL may not be significant for deviations of the order of the resolution of the lithography method.

In order to investigate the PDL of the nanowires due to asymmetry, the eigenmodes of rectangular nanowires with a height of 180 nm and widths ranging from 160 to 200 nm (with rounded corners, as before) were calculated in COM-SOL for three different cladding thicknesses. The results of the simulations are shown in figure 5.8.

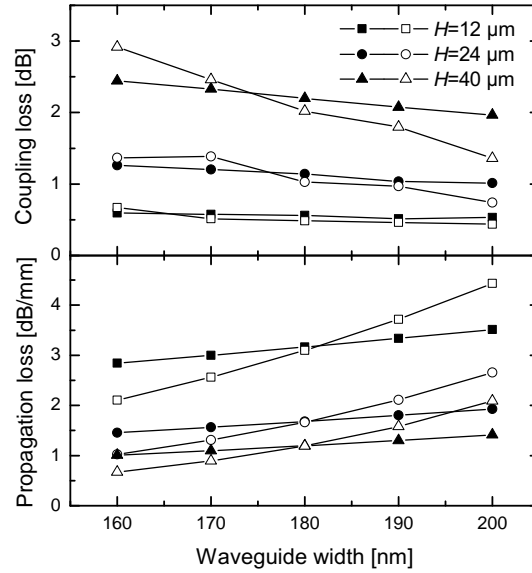


Figure 5.8: The propagation loss and coupling loss in asymmetric nanowire waveguides for the $E^{(0,1)}$ polarized mode (closed symbols) and the $E^{(1,0)}$ polarized mode (open symbols). The height of the wires is fixed at $h = 180$ nm.

The simulations show that only a 5% asymmetry (defined as $(h - w)/h$) can result in substantial polarization dependent loss. The coupling and propagation loss values, however, are affected differently and the variation is also influenced by the cladding thickness. Again, the correct compromise based on the actual device geometry can be used to improve the tolerance to fabrication errors.

The effects of trapezoidal deformation on the polarization dependent loss were also calculated. For a waveguide initially with a square cross-sectional geometry of $180 \text{ nm} \times 180 \text{ nm}$, the propagation loss of the two polarizations was calculated as a function of trapezoidal deformation angle θ (defined in the inset of figure 5.9) while keeping the cross-sectional area fixed. In this case the thickness of the BCB was $20 \text{ }\mu\text{m}$.

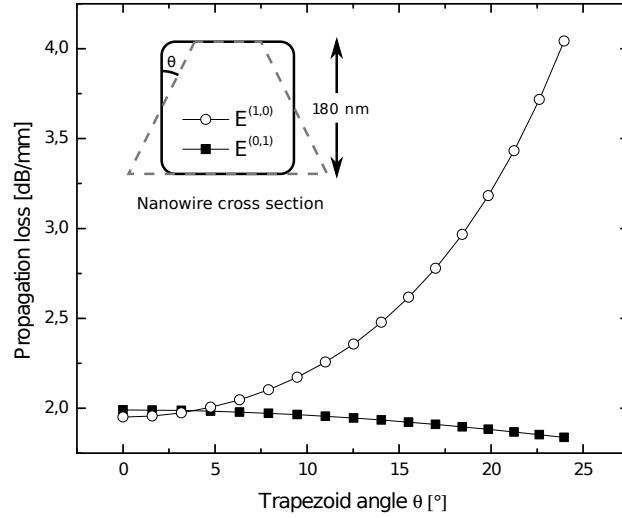


Figure 5.9: Trapezoidal deformation of the nanowire can result in significant polarization dependent loss.

Figure 5.9 shows that the propagation loss of the $E^{(1,0)}$ polarization increases quite quickly with deformation angle, whereas the propagation loss of the $E^{(0,1)}$ polarization remains relatively constant and even decreases slightly. The fabrication of the nanowires is not expected to result in deformations exceeding $\sim 6^\circ$, so the difference in propagation loss for the two polarizations will remain small ($< 0.1 \text{ dB/mm}$) and should not contribute significantly to the PDL in short samples.

5.6 Heated nanowires

Variable optical attenuators made from nanowire waveguides operate on the same principle as their stripe waveguide counterparts [11, 42]. By resistive

heating, the effective indices of the bound modes can be lowered towards the indices of the cladding modes, making it easier to couple the light out of the waveguide. For a $190 \text{ nm} \times 190 \text{ nm}$ gold nanowire waveguide in the middle of a $24 \text{ }\mu\text{m}$ thick BCB cladding the effective mode index was calculated as a function of heating power. As before, the top layer was assumed to be exposed to still air, and the bottom layer supported by a thick silicon substrate, fixed at room temperature. The results are shown in figure 5.10.

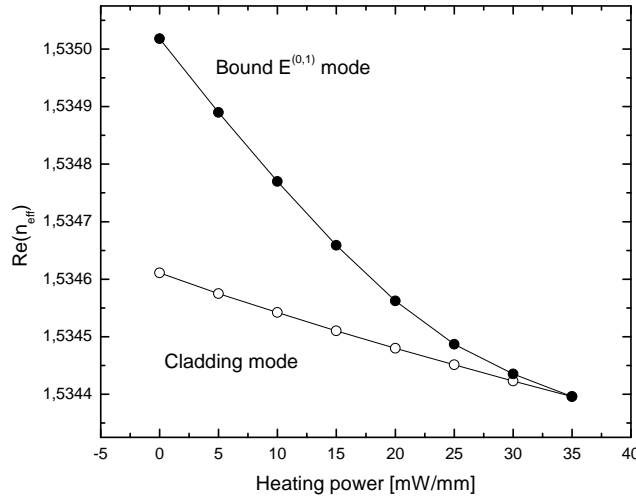


Figure 5.10: The real part of the effective mode index for the $E^{(0,1)}$ polarization versus heating power for a gold nanowire in BCB at $\lambda = 1550 \text{ nm}$. The nanowire corners were symmetrically chamfered to a radius of 5 nm .

As expected, the heating lowers the effective mode indices of the bound modes more quickly than the indices of the cladding modes. The results indicate that for this particular geometry the light is fully expelled from the wire at an applied power of around $30\text{-}35 \text{ mW/mm}$. In fact, at these heating powers the calculated modes had become extremely leaky with a much smaller imaginary part of the effective mode index compared to lower heating powers, indicating that a significant part of the light had started to propagate in the cladding. Figure 5.10 also indicates that a more power efficient variable optical attenuator can be realized using a nanowire than a stripe, since only a $30\text{-}35 \text{ mW/mm}$ of heating is required for full attenuation compared to $40\text{-}55 \text{ mW/mm}$ in the case of the stripe. However, in order to realize temperature independent PDL,

severe demands are placed on the lithography [42].

The influence of heating on the coupling loss and propagation loss was also investigated. Figure 5.11 shows how the coupling loss to a standard single mode fiber with a MFD of $10.5\text{ }\mu\text{m}$ rises with increased power dissipation, whereas the propagation loss decreases due to reduced mode confinement. The insertion loss of waveguides with lengths ranging from 0.1 mm to 5 mm as a function of heating power is also shown. As expected, shorter waveguides present smaller insertion losses, but for waveguides longer than about 3 mm , the insertion loss actually becomes lower for an applied power of 30 mW/mm than when the waveguides are unheated. Although perhaps not a particularly useful effect due to the heavy insertion losses imposed on the signal, it is interesting to note that turning on the power causes more light to be transmitted. Furthermore, from figure 5.11 it can be seen that waveguide lengths of around 3 mm have a power independent insertion loss up to a heating of 20 mW/mm , an effect that can be of benefit to interference modulators.

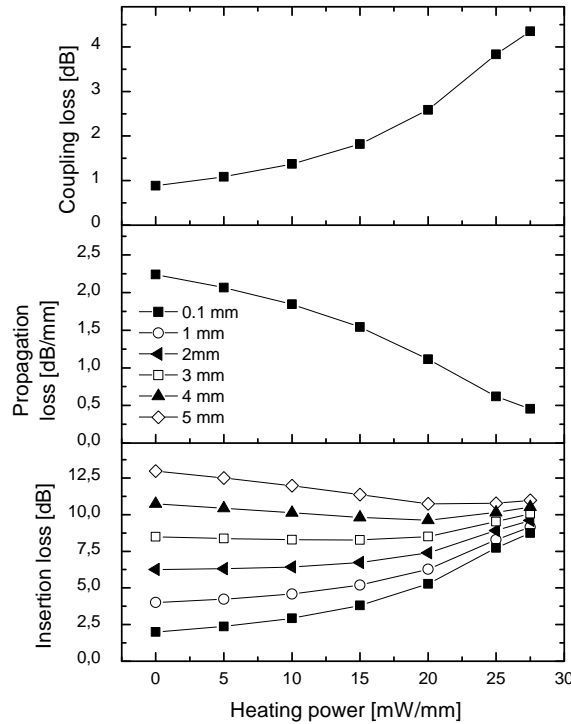


Figure 5.11: Heating the waveguide leads to increased coupling loss and insertion loss. The propagation loss decreases however.

6 Conclusion and discussion

In this thesis the properties of long-range surface plasmon polariton (LR-SPP) stripe and nanowire waveguides and devices were investigated using the finite element method. By simultaneously using the stripes or wires as waveguides and heating elements, the eigenmodes of the structures may be altered in order to realize active waveguide components. Novel integrated optical devices based on single-mode and multi-mode waveguides that have been presented experimentally in the literature have been analyzed in detail, such as variable optical attenuators and directional couplers. Furthermore, a 1×2 optical switch based on a multimode interferometer has been explored.

By optimizing the cross-sectional geometry of stripe waveguides with respect to insertion loss and coupling to a single mode fiber, a minimum insertion loss of 0.88 dB can be realized for a 1 mm long device at the telecommunication wavelength $\lambda = 1550$ nm. In order for an actual device to approach this value however, losses associated with the cladding polymer, scattering from waveguide imperfections, coupling to substrate and facet reflections must be minimized. Similarly, a considerably higher minimum insertion loss of 3.47 dB was obtained for an equally long nanowire waveguide in an unoptimized cladding. However, it was shown that the geometry of the cladding can have a substantial effect on the performance of nanowire waveguides. By correctly choosing the cladding width and thickness, the insertion loss can be reduced to 2.57 dB.

The properties of heat transfer in LR-SPP waveguide components were investigated with special emphasis on the mechanism of attenuation in variable optical attenuators (VOAs). It was shown that by heating waveguides embedded in dielectric claddings with negative thermo-optic coefficients, the real part of the effective mode index of bound modes is reduced. Due to the local nature of the heating, the effective mode indices of cladding modes drop more slowly and LR-SPP waves are therefore more easily scattered into unbound modes. The light in LR-SPP waveguides can therefore be attenuated simply by passing a current through them, enabling the waveguides to be used as variable optical attenuators.

In addition to VOAs, directional couplers and tunable multimode interference devices were also investigated. It was demonstrated that for a 40 μm

wide and 2.45 mm long MMI device consisting of two 4 μm wide electrically isolated heating stripes on either side of a main body with an off-center input waveguide, switching between two output waveguides could be realized for an applied power of 60 mW/mm.

Transient analysis of waveguide heating indicates that response times between 1 and 2 ms can be expected for LR-SPP thermo-optic devices. It was revealed that heating the waveguides under asymmetric cooling conditions increased the coupling loss substantially, but reduced the propagation loss due to decreased mode confinement. In the case of stripe waveguides, the waveguide length was found to play only a minor role in the overall insertion loss at heating currents around 50 mW/mm. Increasing the waveguide length by a factor of 100 (from 0.1 mm to 10 mm) only increased the insertion loss by a modest 1.5 dB, indicating that efficient variable optical attenuators can be realized with short waveguide lengths. The same general behavior of the coupling loss and propagation loss with increased heating power was observed for nanowire waveguides, but the insertion loss of the different device lengths was not found to converge as strongly as for the stripes in the heating range examined. Instead, other effects such as temperature independent insertion loss and insertion loss decreasing with increased temperature, depending on device length, were seen.

The influence of waveguide asymmetry in the form of trapezoidal deformation or a mismatch between the waveguide width and height were also investigated. While the trapezoidal deformation was not found to contribute significantly to polarization dependent loss in short samples for deformations within the expected lithographic tolerances, only a 5% asymmetry between waveguide width and height was found to result in substantial polarization dependent loss.

Although the work presented here has focused on waveguides based on gold stripes or nanowires embedded in BCB, other metals and polymers can also be used. As mentioned before, BCB is chosen because of its simple processing, chemical resistance and relatively high glass transition temperature. By using a polymer with a greater (i.e. more negative) thermo-optic coefficient, the applied power necessary for attenuation or switching would be reduced, leading to more power efficient devices and increased device lifetimes due to decreased electromigration. In addition to gold, silver also has suitable optical properties at telecommunication wavelengths [17], but is prone to oxidation which can render it incapable of guiding SPPs.

As discussed earlier, the main drawbacks of LR-SPP stripe waveguides are the strong polarization dependence and high loss. Even though the problem of polarization can be solved by replacing the stripe with a symmetric square nanowire, the question of the short propagation distances remains. There is currently ongoing work which aims at reducing the propagation loss by placing the waveguides in a gain medium and pulsing it with a laser, but this is not expected to eradicate the loss completely. Keeping that in mind, LR-SPP technology is therefore mainly suited for simple, compact devices while more complex devices requiring longer propagation lengths, significant lateral displacements or multiple functionalities will in all cases exhibit excessive insertion loss compared to other available technologies that will in most cases outweigh possible advantages.

Bibliography

- [1] X. D. Hoa, A. G. Kirk and M. Tabrizian, *Biosensors and Bioelectronics* **23**, 151 (2007)
- [2] S. M. Nie and S. R. Emery, *Science* **275**, 1102 (1997)
- [3] D. Sarid, *Physical Review Letters* **47**, 1927 (1981)
- [4] J. J. Burke, G. I. Stegeman, and T. Tamir, *Physical Review B* **33**, 5186 (1986)
- [5] P. Berini, *Physical Review B* **61**, 10484 (2000)
- [6] R. Charbonneau, P. Berini, E. Berolo and E. Lisicka-Shrzek, *Optics letters* **25**, 844 (2000)
- [7] T. Nikolajsen, K. Leosson, I. Salakhutdinov and S. I. Bozhevolnyi, *Applied Physics Letters* **82**, 668 (2003)
- [8] A. Boltasseva, T. Nikolajsen, K. Leosson, K. Kjaer, M. S. Larsen, and S. I. Bozhevolnyi, *Journal of Lightwave Technology* **23**, 413 (2005)
- [9] T. Nikolajsen and K. Leosson and S. I. Bozhevolnyi, *Applied Physics Letters* **85**, 5833 (2004)
- [10] P. Berini, US patent number 6,741,782 (2004)
- [11] K. Leosson, T. Nikolajsen, A. Boltasseva and S. I. Bozhevolnyi, *Opt. Express* **14**, 314 (2006)
- [12] J. Jung, T. Søndergaard and S. I. Bozhevolnyi, *Physical Review B* **76**, 035434 (2007)
- [13] The Dow Chemical Company, *CYCLOTENE Advanced Electronics Resins - Properties*, retrieved 31/10/2007,
<<http://www.dow.com/cyclotene/solution/index.htm>>

- [14] D. K. Cheng, *Field and Wave Electromagnetics*, 2nd edition (Addison-Wesley, New York, 1989)
- [15] S. A. Maier, *Plasmonics: Fundamentals and Applications* (Springer, Berlin, 2007)
- [16] N. W. Ashcroft and N. D. Mermin, *Solid State Physics* (Brooks Cole, 1976)
- [17] P. B. Johnson and R. W. Christy, *Physical Review B* **6**, 4370 (1972)
- [18] H. Raether, *Surface Plasmons on Smooth and Rough Surfaces and on Gratings* (Springer, 1988)
- [19] J. R. Sambles, G. W. Bradbery, and F. Yang, *Contemporary Physics* **32**, 173 (1991)
- [20] J. R. Krenn, R. Wolf, A. Leitner and F. R. Aussenegg, *Optics Communications* **137**, 46 (1997)
- [21] B. Hecht, H. Bielefeldt, L. Novotny, Y. Inouye and D. W. Pohl, *Physical Review Letters* **77**, 1889 (1996)
- [22] C. S. Desai and T. Kundu, *Introductory Finite Element Method* (CRC Press, 2001)
- [23] G. P. Nikishkov, *Introduction to the Finite Element Method*, 2009 lecture notes. University of Aizu, Japan, retrieved 25/02/2009, <<http://www.u-aizu.ac.jp/niki/feminstr/introfem/introfem.html>>
- [24] R. D. Cook, D. S. Malkus and M. E. Plesha, *Concepts and Applications of Finite Element Analysis*, 3rd edition (Wiley, New York, 1989)
- [25] G. R. Liu and S. S. Quek, *The Finite Element Method: A Practical Course* (Butterworth-Heinemann, 2003)
- [26] COMSOL AB, Sweden <www.comsol.com>
- [27] Comsol Multiphysics, *User's guide for version 3.3*
- [28] P.L. George and H. Borouchaki, *Delaunay Triangulation and Meshing* (Hermes, Paris, 1998)
- [29] The Engineering toolbox, *Air Properties*, retrieved 30/11/2007, <http://www.engineeringtoolbox.com/air-properties-d_156.html>

- [30] eFunda, *The thermal conductivity of gold*, retrieved 30/11/2007,
<http://www.efunda.com/materials/elements/TC_Table.cfm?Element_ID=Au>
- [31] eFunda, *The heat capacity of gold*, retrieved 30/11/2007,
<http://www.efunda.com/materials/elements/HC_Table.cfm?Element_ID=Au>
- [32] A. Modafe, N. Ghalichechian, M. Powers, M. Khbeis and Reza Ghodssi, *Microelectronic Engineering* **82**, 154 (2005)
- [33] N.N. Smirnova, A.V. Markin, I.E. Boronina and M.A. Lopatin, *Thermochimica Acta* **433**, 121 (2005)
- [34] S. Guo, I. Lundstrom, and H. Arwin, *Applied Physics Letters* **68**, 1910 (1996)
- [35] M. Rashidi-Huyeh and B. Palpant, *Physical Review B* **74**, 075405 (2006)
- [36] T. Nikolajsen, K. Leosson and S. I. Bozhevolnyi, *Optics Communications* **244**, 455 (2005)
- [37] Enablence Technologies Inc., *iVOA Integrated Variable Optical Attenuator Array*, retrieved 05/96/2009,
<http://www.enablence.com/media/pdf/enablence_ivoa_datasheet.pdf>
- [38] NeoPhotonics Corporation, *FVOA5000 Compact Variable Optical Attenuator*, retrieved 05/96/2009,
<www.neophotonics.com/product/fvoa5000v7.pdf>
- [39] F. Ladoucer and J. D. Love, *Silica-Based Buried Channel Waveguides and Devices* (Chapman and Hall, 1996)
- [40] L. B. Soldano and E. C. M. Pennings, *Journal of Lightwave Technology* **13**, 615 (1995)
- [41] Photon Design Ltd., UK <<http://www.photond.com/>>
- [42] K. Leosson, T. Rosenzweig, P. G. Hermannsson, and A. Boltasseva, *Opt. Express* **16**, 15546 (2008)